PADERBORN UNIVERSITY

Power Electronics and Electrical Drives
Prof. Dr.-Ing. Joachim Böcker

Paderborn University
Faculty for Computer Science, Electrical Engineering and Mathematics

Department Power Electronics and Electrical Drives (LEA)

Automated FEM Transformer Design for a Dual Active Bridge

in partial fulfillment of the requirements for the degree of

Master of Science

in Electrical Engineering

by: Till Piepenbrock tpiepe@mail.uni-paderborn.de

version date: December 31, 2021

first examiner: Prof. Dr.-Ing. Joachim Böcker
second examiner: Prof. Dr.-Ing. habil. Stefan Krauter
advisor: Nikolas Förster

Eidesstattliche Erklärung zur Masterarbeit

Ich versichere, die von mir vorgelegte Arbeit selbstständig verfasst zu haben. Alle Stellen, die wörtlich oder sinngemäß aus veröffentlichten oder nicht veröffentlichten Arbeiten anderer entnommen sind, habe ich als entnommen kenntlich gemacht. Sämtliche Quellen und Hilfsmittel, die ich für die Arbeit benutzt habe, sind angegeben. Die Arbeit hat mit gleichem Inhalt bzw. in wesentlichen Teilen noch keiner anderen Prüfungsbehörde vorgelegen.

Paderborn, 31.12.2021

Contents

List of Figures

List of Tables

1. Introduction

With increasing shares of renewable energies, there is a rising demand for decentralized systems enabling peak shaving or providing frequency containment reserve. In general, systems with large battery storage are interesting for such smart grid solutions, provided they are able to feed electrical power back into the grid. Uninterruptible Power Supplies (UPS) do have a large battery storage, but usually are not provided with a bidirectional converter topology. As UPS are usually cost intensive and often without use for years, equipping these systems with such a regenerative capability, is also very interesting from the economic point of view. A UPS with bidirectional DC-DC converter is shown in figure 1.1.

In this master thesis a transformer for a Dual Active Bridge (DAB) DC-DC converter is designed. To enable inductive behaviour for Zero Voltage Switching (ZVS) of the used Silicon Carbide (SiC) MOSFETs, the transformer is provided with an integrated leakage path [1]. Within the transformer design, not only the resulting magnetic component is

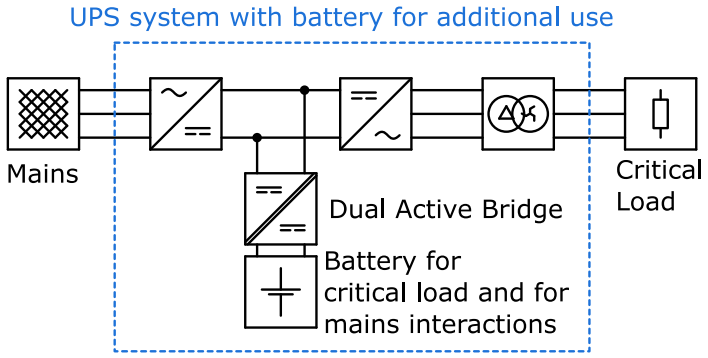

Figure 1.1.: UPS with bidirectional DC-DC converter

of interest, but rather the development of a general design process in an open source software environment. This means, that future development processes of magnetic components can be performed fast and without deeper knowledge of FEM simulations.

The complete design process is performed with the FEM magnetic toolbox (FEMMT), which is an ongoing software project at the Department of Power Electronics and Electrical Drives (LEA) at Paderborn University. FEMMT is capable of drawing core and winding structures from python scripts for (2D radial symmetrical) FEM simulations in an open source environment. In this work, the toolbox is extended by fundamental features, such as an approximation for stranded wires, inductance calculations from the simulation results, core loss models and an analytical reluctance model. (cf. chapter 3)

The full design process of an integrated transformer with a nominal power rating of 2 kW is performed by a combination of prepended analytical and FEM based simulations. To find a loss optimal parameter configuration, a combined global and local grid search algorithm is presented. (cf. chapter 4)

To validate the theoretical simulation results, a laboratory prototype of a DAB including the previously designed integrated transformer is built up. Further, the basic functionality is shown and efficiency measurements of the prototype are taken. (cf. chapter 5)

2. Basic Electromagnetics

The Maxwell Equations describe the behaviour of electromagnetic fields in linear, isotropic and homogeneous materials as follows:[2]

$$\nabla \times \boldsymbol{E} + \frac{\partial \boldsymbol{B}}{\partial t} = 0 \text{ (Faraday's law)} \tag{2.1}$$

$$\nabla \times \boldsymbol{H} - \frac{\partial \boldsymbol{D}}{\partial t} = \boldsymbol{J} \text{ (Maxwell-Ampére law)} \tag{2.2}$$

$$\nabla \cdot \boldsymbol{D} = \rho \text{ (Gauss's law)} \tag{2.3}$$

$$\nabla \cdot \boldsymbol{B} = 0 \text{ (Gauss's law - magnetic)} \tag{2.4}$$

For field simulations of passive magnetic components in power electronics the Maxwell Equations are usually simplified to the magnetoquasistatic (MQS) form. Commercial and free tools such as ANSYS Maxwell and FEMM also use this type of problem formulation. [3][4]

In the MQS form of the Maxwell Equations the electric and magnetic fields are treated as decoupled. This means, the change in time of the displacement current density is neglected [5]. As a consequence, wave propagation is not modelled. Thus the *Maxwell-*

Ampére law (2.2) simplifies to equation

$$\nabla \times \boldsymbol{H} = \boldsymbol{J} \text{ (Maxwell-Ampére law in MQS).} \tag{2.5}$$

By introducing a magnetic vector potential $\boldsymbol{A}$ defined by

$$\boldsymbol{B} = \nabla \times \boldsymbol{A} \tag{2.6}$$

and an electric scalar potential ϕ with

$$\boldsymbol{E} = -\nabla\phi \tag{2.7}$$

the $(\boldsymbol{A}, \phi)$ potential equation

$$\nabla \times \left(\frac{1}{\mu}\nabla \times \boldsymbol{A}\right) + \sigma\frac{\partial \boldsymbol{A}}{\partial t} + \sigma\nabla\phi = \boldsymbol{J}_e \tag{2.8}$$

can be derived. Herein, σ denotes the electrical conductivity and $\boldsymbol{J}_e$ the imprinted current density.[5]

However, during the FEM simulation process a solution of equation 2.8 regarding $\boldsymbol{A}$ and ϕ is calculated. The solution depends on the boundary conditions, geometry, applied excitation and mesh accuracy.

Based on this solution, further field quantities such as magnetic and electric fields can directly be calculated without solving any complex system equations. Depending on the chosen material definitions, the magnetic flux density can either be described in a linear relation to the magnetic field or by a non-linear hysteresis curve. The resulting current density in conductors and core parts are obtained with the material's conductivity. Proximity and skin effect are modelled implicitly. Furthermore, also global quantities such as losses, inductance values and flux linkages are calculated directly from the potential

solution.

As all simulations in this thesis are performed in the frequency domain, the field quantities can be represented with complex Root Mean Square (RMS) pointers according to

$$x(t) = \Re\left\{\sqrt{2}\underline{X}\exp(\mathrm{j}\omega t)\right\}. \tag{2.9}$$

Further, the material relations for the electric and magnetic field and flux density relations are introduced as the complex valued equations

$$\underline{\boldsymbol{B}} = \underline{\mu}\,\underline{\boldsymbol{H}}, \tag{2.10}$$

and

$$\underline{\boldsymbol{D}} = \underline{\varepsilon}\,\underline{\boldsymbol{E}}. \tag{2.11}$$

The current density is calculated with the conductivity σ from the electrical field with

$$\underline{\boldsymbol{J}} = \sigma\,\underline{\boldsymbol{E}}. \tag{2.12}$$

2.1. Inaccuracy of Neglecting Wave Propagation

According to the simplified Maxwell-Ampére law in the MQS simplification, the time derivative of the electric flux density or in other words, the influence of the permittivity's real part is neglected. However, as a consequence of that, no wave propagation is concerned.[5] To investigate, whether this assumption is valid, the relation between the

light speed c, wavelength λ and frequency f is given with

$$c = \lambda \cdot f. \tag{2.13}$$

The vacuum light speed is given with the relation

$$c_0 = \frac{1}{\sqrt{\varepsilon_0 \mu_0}} = 299\,792\,458\,\mathrm{m/s}. \tag{2.14}$$

By a rough calculation, choosing a suitable frequency for a power electronic device with SiC semiconductors of 200 kHz, a vacuum wavelength of 1.5 km can be estimated according to 2.14 and 2.13.

Generally, for materials with a relative permittivity ε_r and a relative permeability μ_r different from one, the light speed is described according to

$$c = \frac{1}{\sqrt{\varepsilon_r \varepsilon_0 \mu_r \mu_0}} = c_0 \frac{1}{\sqrt{\varepsilon_r \mu_r}}. \tag{2.15}$$

By taking into account the reduced light speed in materials, for example a ferrite with a relative permeability and permittivity of 3000 and $100 \cdot 10^3$, the wavelength reduces according to equation 2.15 to about 9 cm. Typically, magnetic component of interest have a maximum dimension of about 5 cm. As this length is in the range of approximately half a wave length, wave phenomena can occur and may lead to higher losses [6]. In this thesis, such wave effects are neglected in the simulations.

3. FEM Simulation Framework: FEMMT

The FEM Magnetic Toolbox (FEMMT) is an open source toolbox, which provides the possibility to deal with several issues along the design process of magnetic components. It is an ongoing project, developed in open source with GitHub as Version Control System (VCS) and started 2021-04-01 at the research group LEA of Paderborn University. In FEMMT all FEM simulations are performed with the open source framework "Open Numerical Engineering LABoratory"[7] (ONELAB) which connects the "three-dimensional finite element mesh generator with built-in pre- and post-processing facilities"[8] (GMSH) and the "General Environment for the Treatment of Discrete Problems"[9] (GetDP). The main function of FEMMT is the possibility to offer an interface to this powerful FEM framework directly from python. This interface enables a parameter based selection of core and winding configurations for combined FEM and analytically based simulations.

At this stage of development, the three magnetic components coil, two-winding transformer and two-winding transformer with dedicated stray path (integrated transformer) are supported. Currently, the problem type is limited to two-dimensional, 2D axisymmetric simulations (cf. figure 3.1). This type of axisymmetric simulation is well suited for the most common core types in single-phase applications, such as "ETD", "PQ" "RM" or "EP" geometries, because of their almost radial symmetrical winding setup. The key benefit of this method is the fast calculation time in a two dimensional mesh. Consequently, this allows many iterations on parameter vectors for optimization problems.

In the python interface, the user does not have to specify any geometric details, but

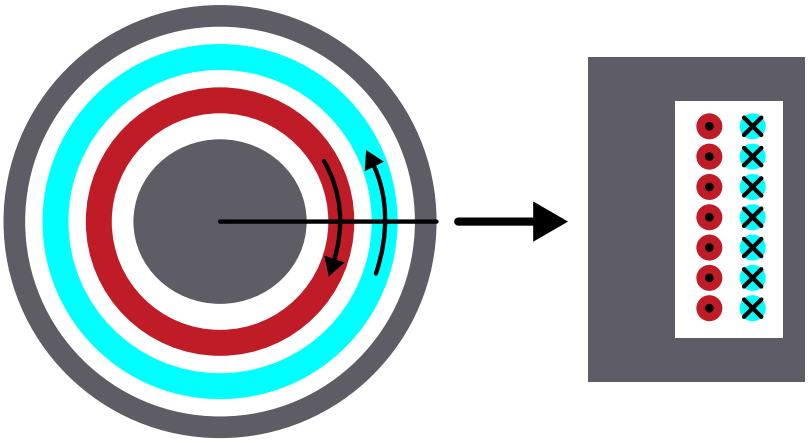

Figure 3.1.: Axisymmetric 2D view of a cylindrically symmetric transformer

can instead simply pass some easily readable parameters to the interface and the whole geometry is built up automatically in the background. For example, an radial symmetric core can be described by its radius of the middle leg, the winding window height and width. Further, air gaps can simply be added by absolute coordinate values or relative to the window height. The windings can be specified by several arrangement options. The problem definition is completed by adding a current excitation to the constructed component. To excite a certain (frequency domain) simulation, the frequency and the primary (and secondary) phase(s) and current amplitude(s) are passed to FEMMT. To give a more intuitive view of FEMMT, in section 3.7 a minimal example of the toolbox is presented.

In the following, some important features of the framework are explained in detail. These features are developed as a part of this thesis, whereas the basic functionality and geometry generation are not part of this thesis.

3.1. Code Structure of FEMMT

The main part of the toolbox is developed in Python. Only the simulation script, the solvers and some material definitions are written in non-python text files. FEMMT

enables the performance of FEM simulations in the code based open source framework ONELAB. Via an Application Programming Interface (API) it is directly possible to interact with the mesh generator GMSH. Further, the solver scripts are written in the finite element solver GetDP, which is an environment to describe discrete physical problems such as the MQS corresponding to equation 2.8. Both, GMSH and GetDP are virtually connected in the ONELAB (Python) module. Within that module the mesh and solver files are sent to a sub client which runs the simulation (cf. listing 3.1). This method works on all common operation systems.

```
import onelab

onelab_client = onelab.client(__file__)
msh_file = onelab_client.getPath(self.path_mesh + 'geometry.msh')
solver = onelab_client.getPath('ind_axi_python_controlled' + '.pro')
onelab_client.runSubClient('myGetDP', mygetdp + ' ' + solver + ' -msh ' +
    msh_file + ' -solve Analysis -v2')
```

Listing 3.1: Run a ONELAB-simulation controlled by python

All data files, shared between the different frameworks, use the ASCII Data File Format. According to figure 3.2, the GetDP solver files can be identified with the file extension ".pro" and the mesh files with ".msh". The result files end with ".pos" for field solutions and ".dat" for global quantities. Typical field solutions of interest are the magnetic flux density and the different loss density distributions, whereas global quantities can be any kind of integrated field solution, such as total losses or mean fluxes, but also inductance values. The resulting fields can be visualized in the GUI of GMSH, whereas the global results can be loaded into python via a loading function of FEMMT.

In FEMMT, the communication between the GetDP solver scripts and python is realized by the file "Parameter.pro" (cf. figure 3.2), which contains all control variables and parameter values for the FEM simulation in the right format. This file is rewritten with every simulation run. The main GetDP file "ind_axi_python_controlled.pro" internally includes the solver file "solver.pro". Herein, "ind_axi_python_controlled.pro"

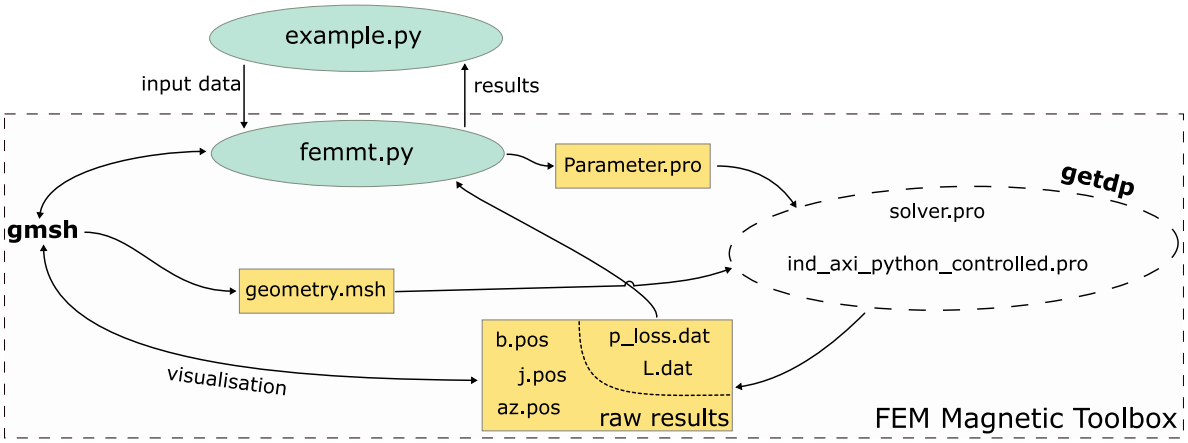

Figure 3.2.: Overview: Code structure of FEMMT

takes the role of the concrete problem description. This means the allocation of the general mesh to physical entities, setting the problem excitation and the material definitions. In the file "solver.pro" the general mathematical formulation of the physical problem is defined and solved. The post processing is again controlled from the file "ind_axi_python_controlled.pro".

From the user's view, a dictionary-based data handling enables user readable raw results and flexible adding of new parameters. From any python file which imports the toolbox ("example.py" in figure 3.2) it is possible to access the functionality of FEMMT. By initializing a magnetic component as an object instance, input parameters can be passed to the toolbox and results can be read back.

To avoid complexity, figure 3.2 only shows the main files and scripts. The complete toolbox contains several additional files with static functions, material definitions and pre-simulation scripts.

3.2. Strands Approximation

Due to the high switching frequencies ($> 100\,\mathrm{kHz}$) in modern power electronics, large losses occur due to small skin depths δ in massive conductors. To overcome this prob-

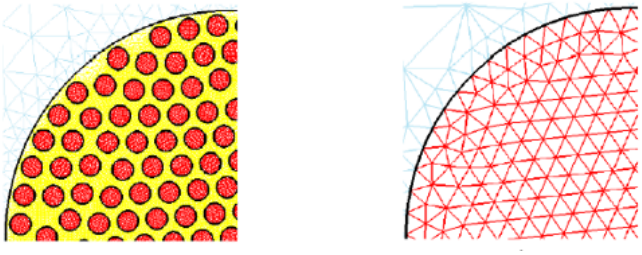

Figure 3.3.: Fine vs. homogenized mesh [10]

lem, High Frequency (HF) stranded wires are widely spread in the range of magnetic components.

For an FEM simulation, the narrow geometries of stranded wires mean a major challenge. A direct method is to implement a very fine mesh, such as shown in the left of figure 3.3. This can lead to millions of mesh elements and an unacceptable long computation time. A better way is to somehow homogenize the mesh and try to estimate the losses due to DC-resistance, skin-effect and proximity-effect by general coefficients in the post-processing. Such a homogenized mesh can be viewed in the right of figure 3.3.

To characterize litz wires in a concrete FEM simulation, some assumptions have to be made. According to figure 3.4, the internal packing of the strands is assumed to be hexagonal. For the description of strands in the real world, it is essential to be able to approximate an arbitrary number of strands. Accordingly, is assumed that round litz wires behave as if they had an internal hexagonal structuring of the strands, but can be described externally as circles.

The basic assumption of modelling stranded conductors by homogenization is, that the current density $\underline{\boldsymbol{J}}$ across the litz wire is distributed equally. Further, a stranded conductor can be identified by a fill factor λ, strand radius r_{strand}, number of strands and a material specific conductivity σ. To describe the relation between the frequency, the strand radius and the conductivity, a reduced frequency can be introduced with

$$X = \frac{r_{\text{strand}}}{\delta} = r_{\text{strand}} \sqrt{f \pi \sigma \mu_0}. \tag{3.1}$$

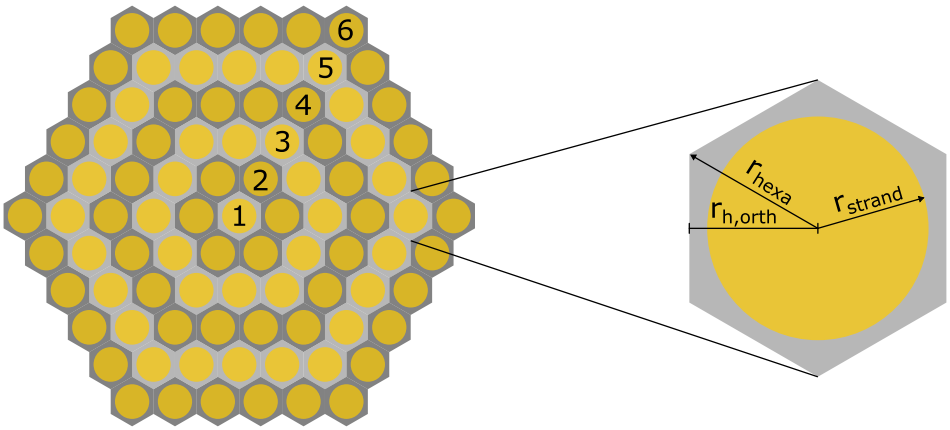

Figure 3.4.: Hexagonal stacking of strands (with 6 layers)

In equation 3.1 the relative permeability of copper is assumed to be 1. To model the losses due to the skin-effect, a complex impedance is defined by

$$\underline{Z}_{\text{skin}} = R_{\text{DC}}(p_I(X) + \text{j}q_I(X)\frac{X^2}{4\lambda}). \tag{3.2}$$

Herein R_{DC} denotes the DC resistance of the litz wire, while $q_I(X)$ and $p_I(X)$ are dimensionless parameters depending on the reduced frequency X. The apparent power density regarding the skin effect $\underline{s}_{\text{skin}}$ can be calculated with

$$\underline{s}_{\text{skin}} = \left(p_I(X)\frac{1}{\sigma} + jq_I(X)\frac{\omega\mu_0}{8\pi}\right)|\underline{\boldsymbol{J}}|^2.[11] \tag{3.3}$$

Analogously, the losses corresponding to the proximity-effect can be modeled by a complex reluctivity ν_{prox}, realized with the two dimensionless parameters $q_B(X)$ and $p_B(X)$ according to

$$\underline{\nu}_{\text{prox}} = \frac{1}{\mu_0}(q_B(X) + jp_B(X)\frac{\lambda X^2}{2}). \tag{3.4}$$

The apparent power density according to the proximity effect can be expressed with

$$\underline{s}_{\text{prox}} = \left(p_B(X) \frac{\omega^2 \lambda \sigma}{4} + j q_B(X) \frac{\omega}{\mu_0} \right) |\underline{\boldsymbol{B}}|^2 .[11] \tag{3.5}$$

The notation of the four dimensionless parameters is subjected to a scheme, where letters p/q indicate the affiliation to the active/reactive power Analogously, the subscripts I/B are chosen in affiliation to the skin/proximity effect.

However, by simulating hexagonal formed stranded conductors with n fully occupied layers, each strand with its specific fill factor, it is possible to extract the dimensionless parameters $q_{\text{I}}(X)$, $p_{\text{I}}(X)$, $q_{\text{B}}(X)$ and $p_{\text{B}}(X)$ [10].

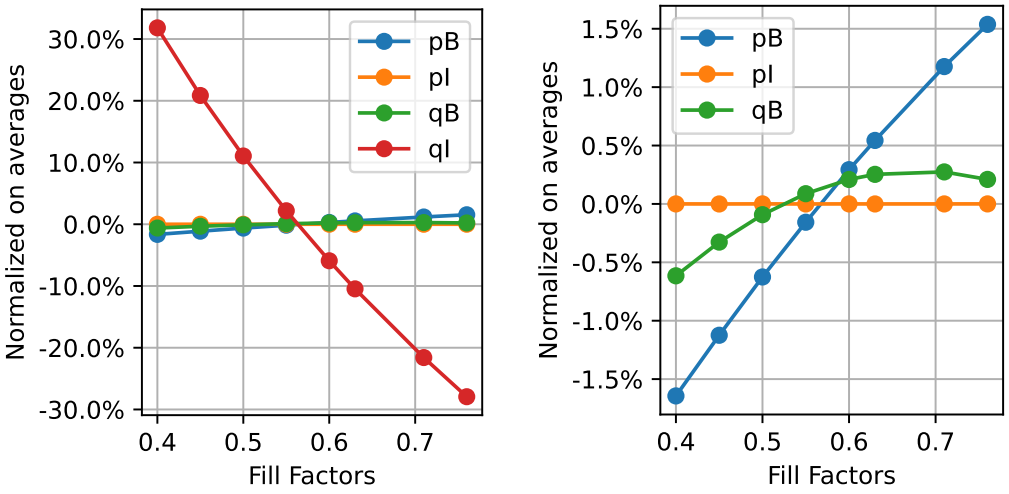

(a) All 4 strand parameters

(b) Zoom on figure 3.5(a): $p_{\text{I}}(X)$, $q_{\text{B}}(X)$ and $p_{\text{B}}(X)$

Figure 3.5.: Dimensionless strand parameters normalized on their averages $(\frac{(*-\bar{*})}{\bar{*}})$ at reduced frequency $X = 1$

The strand parameters vary with the fill factor (cf. figure 3.5) and thus have to be calculated for each fill factor separately. This coefficient generation is implemented in a side simulation, and the results are stored corresponding to their fill factor.

As figure 3.6 shows, the relative deviation of the parameters, depending on the num-

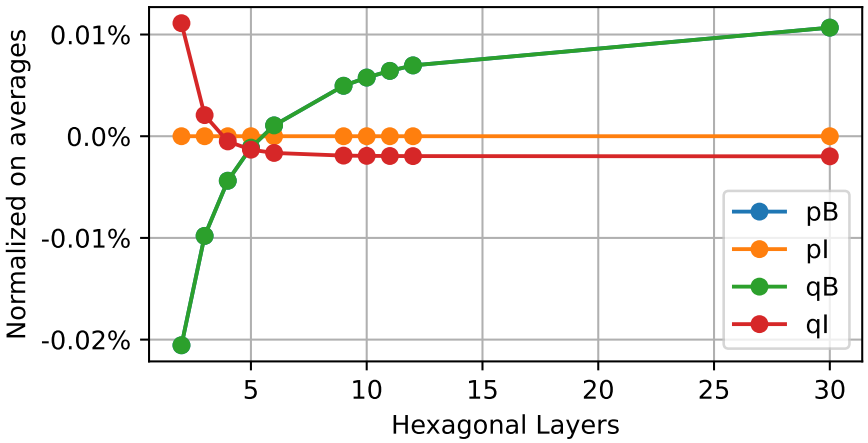

Figure 3.6.: Dimensionless strand parameters normalized on their averages ($\frac{(*-\overline{*})}{\overline{*}}$) at reduced frequency $X = 1$

bers of layers, is below 1 ‰. In terms of a practicable FEM tool, this means to a good approximation, the influence of the number of layers can be neglected. As HF litz wires usually consist of hundreds of strands, this simplification seems to be acceptable.

By combining equations 3.3 and 3.5 and taking into account, that both losses can simply be added, the dissipated power compactly denotes as

$$\begin{aligned} P_{\text{winding}} &= \underbrace{\int \Re\left\{\underline{s}_{\text{skin}}\right\} \,\mathrm{d}V}_{P_{\text{skin}}} + \underbrace{\int \Re\left\{\underline{s}_{\text{prox}}\right\} \,\mathrm{d}V}_{P_{\text{prox}}} \\ &= \int \left(p_I(X) \frac{1}{\sigma} |\underline{\boldsymbol{J}}|^2 + p_B(X) \frac{\omega^2 \lambda \sigma}{4} |\underline{\boldsymbol{B}}|^2 \right) \mathrm{d}V. \text{[11]} \end{aligned} \tag{3.6}$$

To verify the applied homogenization approach, a comparison with the open source tool FEMM is performed. For that purpose, the losses of litz wires in a typical inductor example are determined in FEMM and ONELAB. The fill factor of a litz wire with a strand diameter of 100 µm and 9 layers, which equals 271 single strands, is varied from $40 - 60\,\%$. As figure 3.7 shows, both simulation results match each other with a relative deviation of less than 1 %. Due to the implemented homogenization approach, very fast

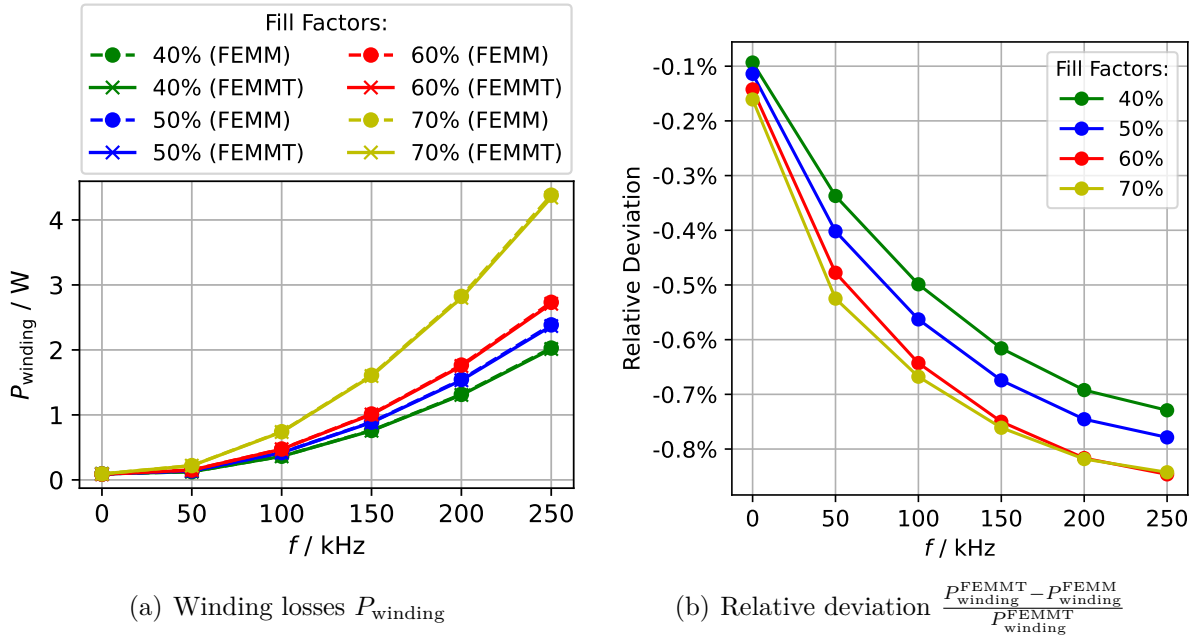

(a) Winding losses P_{winding}

(b) Relative deviation $\frac{P_{\text{winding}}^{\text{FEMMT}} - P_{\text{winding}}^{\text{FEMM}}}{P_{\text{winding}}^{\text{FEMMT}}}$

Figure 3.7.: Comparison of the conductor losses in a typical coil assembly between FEMMT and FEMM: The fill factors and thus the resulting radii are varied with a fixed number of 271 strands with a diameter of 100 µm.

simulations of stranded conductors with a precise loss estimation are realized.

3.2.1. Practical Characterization of Litz Wires

The presented approach of homogenizing stranded conductors needs the definition of "real" Litz Wires from sellers. Generally, a litz wire is characterized by the strands and the isolation. FEMMT only offers the possibility to define the pure (homogenized) strand parameters. To define litz wires in an FEM model, three types of parametrization can be used. This is because one parameter out of litz diameter, fill factor, number of strands and strand diameter can be calculated implicitly out of the other three.

The isolation between common and counter windings can be set according to figure 3.8. It is possible to describe the insulation of the strands by three parameters, where iso_{11} and iso_{22} describe the insulation between the primary and secondary windings to

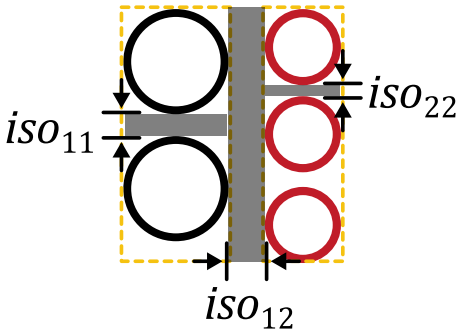

Figure 3.8.: Isolation of adjacent windings

themselves respectively. The parameter iso_{12} characterizes the insulation between both windings and equals the sum of iso_{11} and iso_{22} if no additional isolation is needed. A further isolation between the windings in form of a dedicated barrier can simply be added to the parameter iso_{12}. At this stage of development, the FEM simulation simply treats all isolations as air.

3.3. Inductance Estimation by Simulation

An essential part of the toolbox is the possibility to calculate exact inductance values from simulation results. In case of a two winding transformer the inductance matrix

$$\boldsymbol{L} = \begin{bmatrix} L_{11} & M \\ M & L_{22} \end{bmatrix} \tag{3.7}$$

has to be determined. The inductance matrix is described by the following three parameters:

- Primary self inductance L_{11}
- Secondary self inductance L_{22}
- Mutual inductance M

The determination of the inductance parameters via FEM simulation can be carried out analogous to the practical open circuit test. To calculate the primary self-inductance, only a current in the primary winding is excited, whereas the secondary's current is set to be zero. For the secondary self-inductance the procedure is executed vice versa. [12] The mutual inductance can be calculated from the flux linkages, explained in detail in section 3.3.3.

3.3.1. Inductance Calculation from the Magnetic Field Energy

In general, the self-inductance of a conductor loop is defined by the stored magnetic field energy E_n in the in infinite volume V_{inf} with

$$E_n = \frac{1}{2} \iiint_{V_{\text{inf}}} \boldsymbol{H}\, \boldsymbol{B}\, \mathrm{d}V = \frac{1}{2} \iiint_{V_{\text{inf}}} \frac{(\nabla \times \boldsymbol{A})\,(\nabla \times \boldsymbol{A})}{\mu_0 \mu_r}\, \mathrm{d}V = \frac{1}{2} L_{nn} |I_n|^2 \,, n = \{1, 2\} \tag{3.8}$$

Thus, the self-inductance can be calculated with the magnetic field energy by rearranging equation 3.8 to

$$L_{nn} = \frac{2E_n}{I_n^2} \,, n = \{1, 2\}.[12] \tag{3.9}$$

3.3.2. Inductance Calculation from the Magnetic Flux

A second approach for the simulative calculation of inductances is defined directly from the induced magnetic flux Φ_{mn} penetrating the conductor. In the simulation environment of FEMMT all global and field quantities are calculated directly from the MQS potentials $\boldsymbol{A}$ and ϕ. For a winding m with an infinitesimal small cross section, the magnetic flux

caused by winding n, penetrating the loop is given by

$$\Phi_{mn} = \oint \boldsymbol{A}_n \, \mathrm{d}\boldsymbol{r}. \tag{3.10}$$

Obviously, in the FEM simulation the cross section of each conductor has a certain value. According to that, equation 3.10 can be generalized in such way, that the mean flux penetrating each loop and the conductor itself is taken into account. The flux linkage Φ_{mn} can be denoted according to

$$\Phi_{mn} = \frac{1}{A_m} \sum_m \int_{V_m} \frac{\boldsymbol{j}_m}{|\boldsymbol{j}_m|} \boldsymbol{A}_n \, \mathrm{d}r_m \tag{3.11}$$

with $m = \{1, 2\}$ and $n = \{1, 2\}$. Herein, $\frac{\boldsymbol{j}_m}{|\boldsymbol{j}_m|}$ defines the positive direction of the current density in the loop m. This only is a convention and can either be defined in or against the winding direction. A_m defines the cross section of a single conductor of winding m.[13]

Unlike to the inductance calculation from the magnetic field energy (cf. equation 3.11), it is possible to determine not only the self induced fluxes, but also the flux linkage between primary and secondary winding. To avoid confusion, in the following subsequent definitions for flux linkages will be used:

- Φ_{11}: generated by I_1, induced in primary winding
- Φ_{21}: generated by I_1, induced in secondary winding
- Φ_{12}: generated by I_2, induced in primary winding
- Φ_{22}: generated by I_2, induced in secondary winding

All four flux linkages can be extracted from the two mentioned simulations, each with terminals open on one side. For the inductance values according to the direct calculation

from the magnetic flux, it holds

$$L_{mn} = \frac{\Phi_{mn}}{I_n}\,. \tag{3.12}$$

with $m = \{1, 2\}$ and $n = \{1, 2\}$.

In practical simulations the self-inductance values calculated by flux and magnetic field energy can slightly deviate from each other. This is due to bounded accuracy of the simulation, but practically negligible. Moreover, both ways of calculation allow a simple cross validation of the FEM simulation.

3.3.3. Determination of the Equivalent Circuit Parameters

With the four flux linkages, coupling factors can be calculated as

$$K_{12} = \Phi_{12}/\Phi_{22} \tag{3.13}$$

and

$$K_{21} = \Phi_{21}/\Phi_{11}. \tag{3.14}$$

The geometric mean of the coupling factors follows with

$$k = \sqrt{K_{12}K_{21}} \tag{3.15}$$

and directly gives the counter inductance

$$M = k\sqrt{L_{11}L_{22}}.[12] \tag{3.16}$$

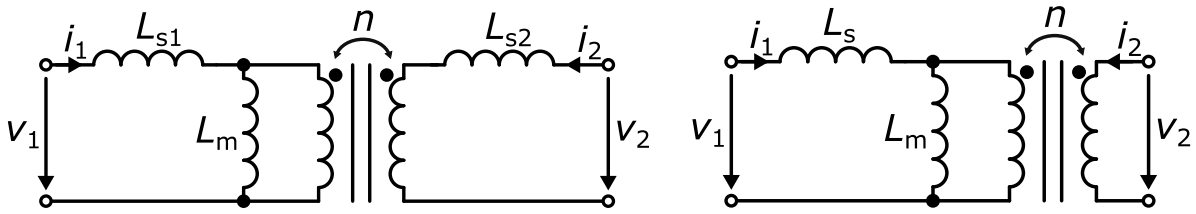

(a) T-ECD with two stray inductances

(b) T-ECD primary side concentrated

Figure 3.9.: Equivalent circuit diagrams of transformers.

Within the counter inductance, the inductance matrix is fully determined. The transformer's behaviour can now be modelled in various electric circuit diagrams such as a T -(shaped) Equivalent Circuit Diagram (T-ECD). Two common variations of the T-ECD are directly included in FEMMT.

As figure 3.9(a) shows, the equivalent circuit is described by the primary and secondary stray inductances (L_{s1}, L_{s2}), the (primary) main inductance L_m and the transformation ratio n. As the equivalent circuit diagram is described by parameters, where the winding matrix only has three parameters, the system is overdefined. Thus, one parameter can be set to an arbitrary value.

A common way to fix one value is to choose the transformation ratio equal to the turns ratio $n = N_1/N_2$. This is a very practicable approach for transformers with coupling factors $k \approx 1$, because then the turns ratio equals in good approximation the voltage ratio.[12]

Another practicable assumption is, to choose the transformer ratio $n = M/L_{22}$ [12]. This leads to a primary concentrated stray inductance L_s shown in figure 3.9(b). After this simplification, only one stray inductance remains. Especially for integrated transformers a certain stray inductance is welcome and usually must be achieved with high accuracy.

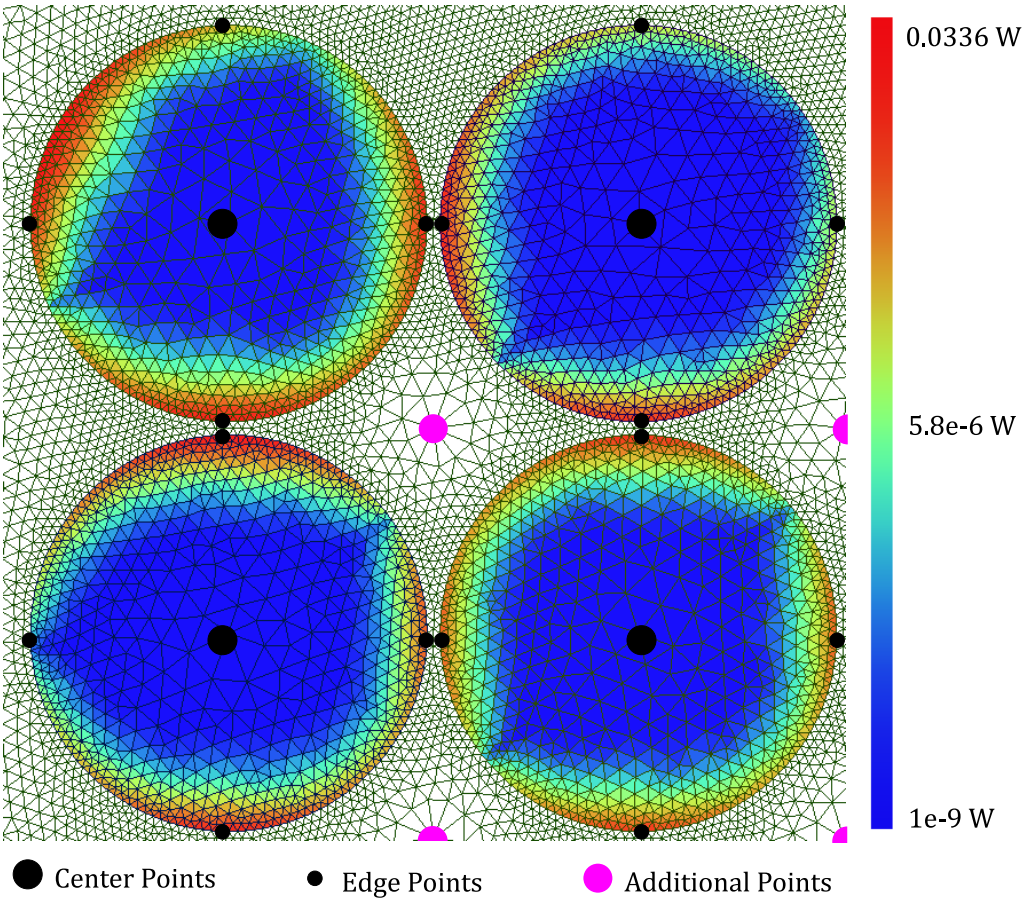

Figure 3.10.: Winding losses of a solid conductor in a skin based mesh with subsequently inserted point coordinates

3.4. Skin Based Meshing

Meshing is the basis of a precise FEM simulation. To only aim very precise results, a homogeneous, but very fine, mesh would be sufficient. In terms of a time-efficient simulation, this way of meshing is not practicable. Therefore, FEMMT makes use of a skin depth based mesh, realized by taking into account the skin depth as a reference for the meshing of solid conductors.

In GMSH round conductors can be defined by five points, one in the center and four points placed at 3, 6, 9 and 12 o'clock (cf. figure 3.10). To applicate the skin-effect

precisely, a heterogeneity of a coarse mesh inside the conductor and a fine resolution on the edge is desirable. This is realized by choosing a coarse resolution defined in the center point and a smaller resolution corresponding to the skin depth for the four other points. To avoid unnecessary fine meshing between the conductors, further points are placed to locally reduce the mesh resolution.

This method is only applied for solid conductors. As the stranded conductors are modelled by a homogeneous approximation, a skin based mesh is not necessary.

3.5. Simulation of Core Losses

A very crucial task in transformer design is the estimation of core losses. In FEMMT the core losses can either be calculated via complex material parameters or with the empirical Steinmetz equation. Both methods are presented in sections 3.5.1 and 3.5.2.

Further, it can be distinguished between local and analytical methods. Analytical methods assume a uniform magnetic flux density in each part of the core. If the total flux in each part of the core is known, for these methods not necessarily an FEM simulation is needed. But obviously, there are benefits of taking the local flux distribution into account. Especially in the inner corners of cores higher flux densities can be expected. Although in this thesis neglected, in future works maybe full wave equations shall be taken into account. This leads to even more heterogeneous magnetic flux density distributions [6]. To overcome this problem, local loss estimations will become indispensable.

3.5.1. Complex Core Parameters

The introduction of complex core parameters is a frequency domain approach to calculate the core losses. The complex permeability and permittivity are defined by $\underline{\mu} = \mu' - \mathrm{j}\mu''$

and $\underline{\varepsilon} = \varepsilon' - \mathrm{j}\varepsilon''$. According to [6] the theorem of Poynting says

$$-\oint_{\delta V} \underbrace{(\underline{\boldsymbol{E}} \times \underline{\boldsymbol{H}}^*)}_{\text{Poynting vector}} \, \mathrm{d}S = \int_V \left[\underbrace{(\kappa + \omega\varepsilon'')|\underline{\boldsymbol{E}}|^2}_{\text{el. loss}} + \underbrace{\omega\mu''|\underline{\boldsymbol{H}}|^2}_{\text{mag. loss}} \right] \mathrm{d}V + \mathrm{j}\omega \int_V \underbrace{\left(\mu'|\underline{\boldsymbol{H}}|^2 - \varepsilon'|\underline{\boldsymbol{E}}|^2\right)}_{\text{field energy}} \mathrm{d}V. \tag{3.17}$$

With the following substitution

$$\tilde{\underline{\varepsilon}} = \varepsilon' - \mathrm{j}\left(\varepsilon'' + \frac{\kappa}{\omega}\right), \tag{3.18}$$

the eddy current loss density follows with

$$p_{eddy} = -\omega \Im(\tilde{\underline{\varepsilon}}) |\underline{\boldsymbol{E}}|^2. \tag{3.19}$$

The hysteresis loss density can be expressed via

$$p_{hysteresis} = -\omega \Im(\underline{\mu}) |\underline{\boldsymbol{H}}|^2 .[6] \tag{3.20}$$

With formulas 3.19 and 3.20, the core losses can be expressed locally (in every mesh cell) in the post-processing of the FEM simulation. Usually the two material parameters $\underline{\mu}$ and $\tilde{\underline{\varepsilon}}$ are not given by the core manufacturers. In FEMMT the core parameters are taken from [6].

As the measured curves are subjected to some non-idealities, curve fitting is needed to make the curves usable for a GetDP-interpolation function. To keep it simple, the exemplary characterization process of a core material, is shown for N95. Figure 3.11 shows the relative permeability $\mu_r = \left|\underline{\mu_r}\right|$. To allow fast and non-iterative solving, the relative permeability is assumed to be independent of the magnetic flux density. Thus, μ_r is set to the constant value of 3000.

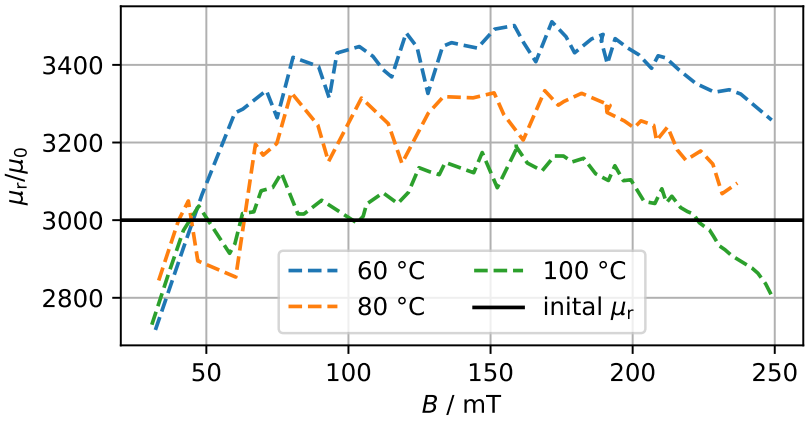

Figure 3.11.: Relative permeability for N95

Quite different is the loss angle of N95, which strongly depends on the magnetic flux density. [6] To directly calculate the hysteresis losses corresponding to equation 3.20 in the in the post processing, a curve $(\frac{\mu''}{\mu_0})(\hat{b})$ eliminated by the measurement inaccuracies is stored in a GetDP readable data file. Figure 3.12 shows this relation for the frequencies 200 and 300 kHz. Further, in the solver script itself, a linear interpolation between those curves makes it possible, to realize the loss estimation for frequencies between the measurements, that have been performed.

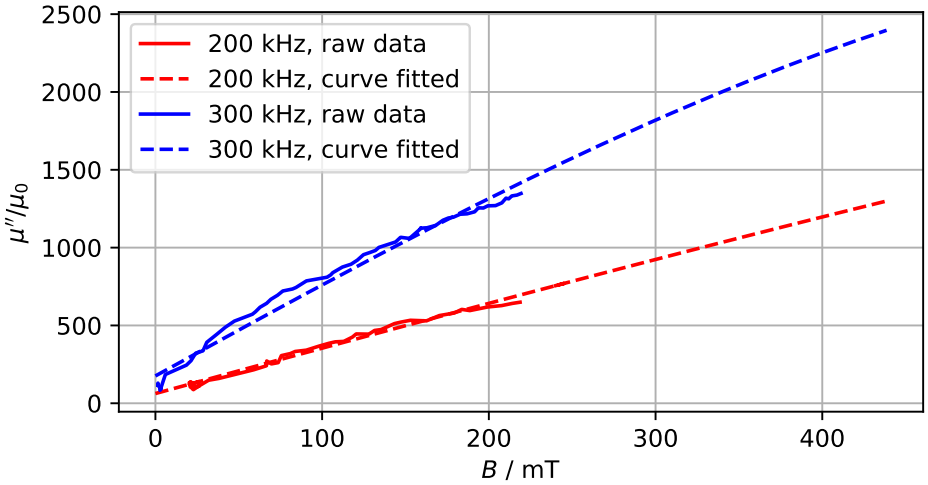

Figure 3.12.: Imaginary part of the complex permeability for N95

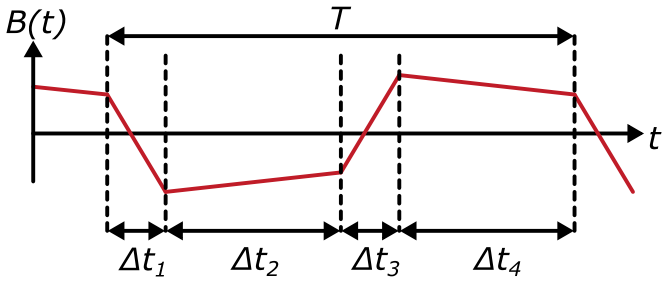

Figure 3.13.: Piece-wise linear magnetic flux density

The procedure to extract the permittivity data works out analogously and can be retraced in [6]. At this stage of development, the temperature dependency is neglected. In future developments, more materials with extended data shall be included into FEMMT. For this purpose, a database seems to be the most appropriate way to deal with these different curves.

3.5.2. Improved Generalized Steinmetz Equation

Opposite to the complex core parameters, the improved Generalized Steinmetz Equation (iGSE) is an empirical formula, that generally describes all loss characteristics without an assignment to the certain phenomena. The power loss density according to the iGSE is described with the three parameters k, a and b according to

$$P_{\mathrm{iGSE}} = \frac{1}{T}\int_0^T k_i \left|\frac{dB}{dt}\right|^a (\Delta B)^{b-a}\,\mathrm{d}t. \tag{3.21}$$

Herein, ΔB denotes the peak-to-peak flux density and k_i is given with

$$k_{\mathrm{i}} = \frac{k}{(2\pi)^{a-1}\int_0^{2\pi}|\cos\theta|^a 2^{b-a}\,d\theta}. \text{ [14]} \tag{3.22}$$

By neglecting saturation effects the relation between current and magnetic flux density can be assumed to be proportional by the permeability. Thus, piece-wise linear currents

$i(t)$ lead to piece-wise linear magnetic flux densities $b(t)$ (cf. figure 3.13) and the iGSE can be simplified to

$$P_{\mathrm{iGSE}} = \frac{1}{T} k_i (\Delta B)^{b-a} \sum_i \left| \frac{(\Delta B)_i}{(\Delta t)_i} \right|^a (\Delta t)_i. \tag{3.23}$$

Assuming linear material behaviour, the magnetic flux density $B(x, y, z, t)$ can be split into a time constant field distribution across the core geometry $k(x, y, z)$ and the time dependent excitation current $i(t)$ with

$$B(x, y, z, t) = k(x, y, z) i(t). \tag{3.24}$$

Following equation 3.24, the local distribution of the magnetic flux density can be determined by a single frequency domain simulation with the peak current value.

By using the location-dependent magnetic flux density in the iGSE, FEMMT is able to determine the Core Losses in every single mesh element. With the post processing functions it is possible to directly integrate the Core Loss Density to a local or global quantity (losses in the mesh element or total losses). The integration is performed efficiently with built-in functions of GMSH and GetDP.

3.5.3. Limits of FEM Based Core Loss Approaches

Currently the complex material parameters are only measured for sinusoidal excitation. Thus, the hysteresis loss estimation with complex material parameters is restricted to waveforms with a dominating fundamental content. Differently, the eddy current losses of non sinusoidal curve forms can be estimated with a summation of the losses corresponding to each harmonic.

With the iGSE, non sinusoidal magnetic flux densities can be treated. Herein, the quality of the available empirically determined coefficients is most problematic. Espe-

cially for in-house constructed cores, the losses may differ from standard topologies.

Beyond their individual drawbacks, both approaches have a restriction in common for the FEM based local approach. Due to their implementation in the frequency domain, both approaches are limited to a locally uniform time dependence of the magnetic flux in the core. In order to that, only the losses of non-branched magnetic circuits can be handled with this way of implementation. As figure 4.5 shows, branches in the magnetic circuit lead to deviating flux forms in different parts of the core, if non-sinusoidal currents are present. An alternative analytical approach is presented in 4.2.2.

3.6. Reluctance Model

Besides the FEM features, analytical models are an essential part of FEMMT. These models allow very fast calculations, especially for pre-dimensioning air gaps in optimization routines. A detailed motivation for analytical models is given in section 4.1.3. In this thesis, the implementation of a reluctance model for a transformer with a dedicated stray path is presented in detail. Such a dedicated stray path can be used to integrate a certain stray inductance directly into the transformer. In the following, such a magnetic component is called an integrated transformer. The applied methods and formulas can be reused in a simplified way for analytical models of simple chokes and transformers.

3.6.1. Magnetic Circuit Basics

A reluctance model is a (simple) magnetic circuit consisting of discrete magnetic resistances arranged in closed loop paths. Analogously to electrical circuits, the magnetic flux ϕ corresponds to the electrical current i and the magnetomotive force (MMF) ψ to the voltage v. Further, the (magnetic) reluctance complies with the electrical resistance. In this circuit simplification the influence of the exact conductor positioning as well as non homogeneous flux distributions along the magnetic conductors are neglected.

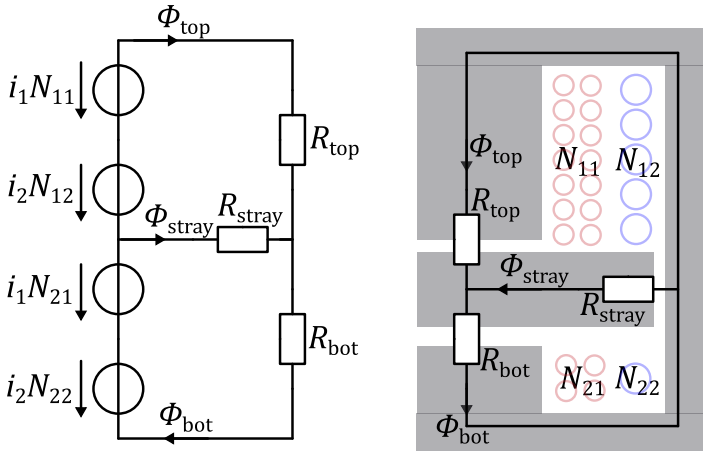

Figure 3.14.: Magnetic equivalent circuit of a transformer with integrated stray path

3.6.2. Reluctance Model for an Integrated Transformer

An integrated transformer can generally be described by a magnetic equivalent circuit consisting of four magnetic voltage sources and three discrete reluctances.[1]

According to figure 3.14, three fluxes namely ϕ_{top}, ϕ_{bot} and ϕ_{stray} are the unknowns of the system. Due to Kirchhoff's law, it holds

$$\phi_{\text{stray}} = \phi_{\text{bot}} - \phi_{\text{top}}. \tag{3.25}$$

As [6] shows, the reluctance model can be described with the linear equation system

$$\begin{bmatrix} R_{\text{top}} + R_{\text{stray}} & -R_{\text{stray}} \\ -R_{\text{stray}} & R_{\text{bot}} + R_{\text{stray}} \end{bmatrix} \begin{bmatrix} \phi_{\text{top}} \\ \phi_{\text{bot}} \end{bmatrix} = \begin{bmatrix} N_{11} & N_{12} \\ N_{21} & N_{22} \end{bmatrix} \begin{bmatrix} i_1 \\ i_2 \end{bmatrix} \tag{3.26}$$

and by introducing a matrix notation with

$$\boldsymbol{R\phi} = \boldsymbol{Ni}, \tag{3.27}$$

$$\boldsymbol{\phi} = \boldsymbol{R}^{-1}\boldsymbol{N}\boldsymbol{i} \tag{3.28}$$

and

$$\boldsymbol{\psi} = \boldsymbol{N}^{\mathrm{T}}\boldsymbol{\phi} = \boldsymbol{N}^{\mathrm{T}}\boldsymbol{R}^{-1}\boldsymbol{N}\boldsymbol{i}. \tag{3.29}$$

To enable a pre-dimensioning of the air gap parameters, the three goal reluctance values must be determined. With given winding numbers and goal inductance matrix, the reluctance matrix $\boldsymbol{R}$ can be calculated according to

$$\boldsymbol{R} = \boldsymbol{N}\boldsymbol{L}^{-1}\boldsymbol{N}^{T}. \tag{3.30}$$

At this point, all parameter configurations that result in a negative reluctance value can be omitted and no further investigation is required. This is very useful to exclude non-realizable parameter sets from an optimization routine.

To calculate the resulting fluxes, equation 3.28 is used. Generally, there are combinations of the winding matrix $\boldsymbol{N}$ being singular. Due to equation 3.30, this leads to singular and thus not invertible reluctance matrices $\boldsymbol{R}$. To generally show, a matrix multiplication, including a singular matrix, always gives another singular matrix, an arbitrary singular matrix $\boldsymbol{A}$ and a regular matrix $\boldsymbol{B}$ are assumed. For $\boldsymbol{A}$ it exists a vector $\tilde{\boldsymbol{x}} \neq \boldsymbol{0}$ which holds $\boldsymbol{A}\tilde{\boldsymbol{x}} = 0$ and thus $\boldsymbol{B}\boldsymbol{A}\tilde{\boldsymbol{x}} = \boldsymbol{B} \cdot 0 = 0$.

Consequently, singular stray matrices lead to singular reluctance matrices according to equation 3.30. To meet the condition for singularity with $\det(\boldsymbol{R}) = 0$ it must hold $R_{11}R_{22} = R_{21}R_{12}$ or to put it differently

$$R_{\mathrm{top}}R_{\mathrm{stray}} + R_{\mathrm{bot}}R_{\mathrm{stray}} + R_{\mathrm{bot}}R_{\mathrm{top}} = 0. \tag{3.31}$$

Equation 3.31 can be satisfied only with some reluctance value being negative or

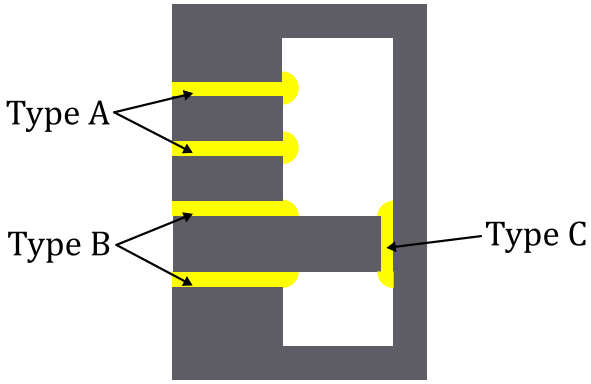

Figure 3.15.: Types of air gaps with indicated fringing fields

choosing two reluctances to be zero. The first approach is physically not possible. The second approach leads to a magnetic equivalent circuit with only one reluctance value. This corresponds to an idealized transformer reluctance model without stray fields. Further, the singularities' condition $N_{11}/N_{12} = N_{21}/N_{22}$ leads to equal turn ratios in both winding windows. As a practical consequence for an integrated transformer, singular cases can be discarded during the design process.

3.6.3. Air Gap Characterization Including Fringing Effects

Due to the usage of highly permeable materials and for simplification, the reluctance values of the core itself are neglected. This means, that the reluctance values shall be chosen only according to the air gaps. Especially for small air gaps, this can lead to certain inaccuracies. As the presented analytical reluctance model is mainly used for the purpose of pre-estimating the transformer behaviour, an FEM based inductance calculation according to section 3.3 is essential for the exact dimensioning of the air gaps.

In a typical dimensioning task, the only air gap parameter to calculate, is the length. As the core parameters are usually given by parametrization and the core's form is known, also the air gap's cross-sections are known.

For air gaps with a small length to area ratio it is sufficient to assume a homogeneous

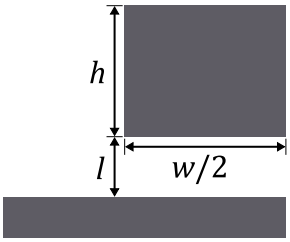

Figure 3.16.: Basis air gap configuration R'_{basic}

field. This assumption does not longer hold for increasing air gap lengths, as fringing effects of the magnetic flux density become superficial. For an integrated transformer, figure 3.15 shows the typical widened cross sections evoked by fringing magnetic fluxes. It can be distinguished between three different types of air gaps (cf. figure 3.15).

- Type A: Air gap between to equally sized tablets
- Type B: Air gap between a tablet and a tablet with a significantly larger cross section
- Type C: Air gap between a cylinder surface and a cylinder surface with a significantly larger height

A proven method to analytically deal with the fringing effects of such different air gap geometries is presented by using the Schwarz-Christoffel transformation in [15]. In this section, the case-specific implementation of fringing air gaps using this general approach is applied to the radial symmetric model of an integrated transformer.

All three air gap types (cf. figure 3.15) can be represented by series and parallel connection of the basic geometry according to figure 3.16 with

$$R'_{\text{basic}} = \frac{1}{\mu_0 \left[\frac{w}{2l} + \frac{2}{\pi}\left(1 + \ln\frac{\pi h}{4l}\right)\right]}.[15] \tag{3.32}$$

As figure 3.16 implies, the basis air gap configuration is equivalent to a quarter of the air gap type A and half of types B and C. Consequently, the reluctance of air gap type A

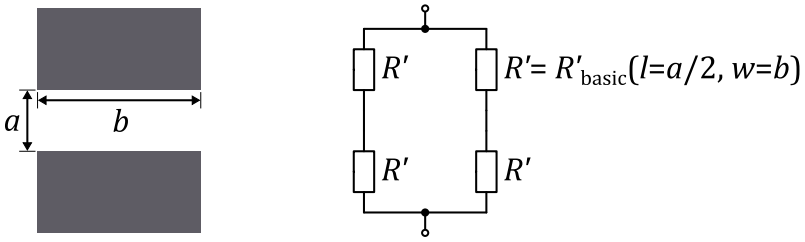

(a) Type A

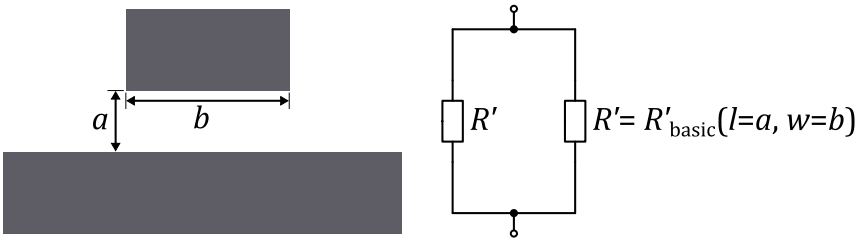

(b) Type B and Type C

Figure 3.17.: Equivalent circuits of 1D air gap reluctances [15]

is given by the parallel connection of two serial connected basic reluctances R'_{basic} with the input parameters $L = a/2$ and $w = b$ (cf. figure 3.17(a)).

The air gap types B and C can be represented by a parallel connection of the basic reluctance R'_{basic} with the input parameters $L = a$ and $w = b$ (cf. figure 3.17(b)).

Herein, the fringing only in one coordinate direction is concerned. From these 1D reluctance values, fringing factors can be established with

$$\sigma_u = \frac{R'_{vw}}{\frac{a}{\mu_0 b}}, \tag{3.33}$$

where u can represent the three Cartesian coordinates as well as the radial coordinate in a cylindrical coordinate system. As a consequence, the fringed air gap reluctance of round shaped cross sections (type A and B) can be calculated with the corresponding

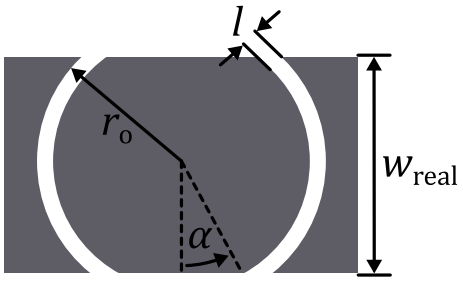

Figure 3.18.: Parametrization of a typical ferrite core geometry with stray path.

the radial fringing factor σ_A or σ_B according to

$$R_{\mathrm{A/B}} = \sigma^2_{\mathrm{A/B}} R_{\mathrm{ideal}} = \sigma^2_{\mathrm{A/B}} \frac{l}{\pi \mu_0 r^2}. \tag{3.34}$$

In equation 3.34 the ideal (no fringing) air gap reluctance is simply multiplied with the squared radial fringing factor either according to figure 3.17(a) or 3.17(b). Due to the radial axial symmetry of the FEM simulation, for air gap type C fringing is only relevant in one dimension. The reluctance value of an air gap between two cylindrical surfaces without fringing can be expressed by

$$R_{\mathrm{cyl,\ ideal}} = \frac{\ln \frac{r_o}{r_o - l}}{2\pi \mu_0}.[6] \tag{3.35}$$

Finally, the air gap reluctance with one dimensional fringing included can be expressed by

$$R_{\mathrm{cyl}} = \sigma_y R_{\mathrm{cyl}}. \tag{3.36}$$

Equation 3.35 can be extended for incomplete axially symmetrical geometries (cf.

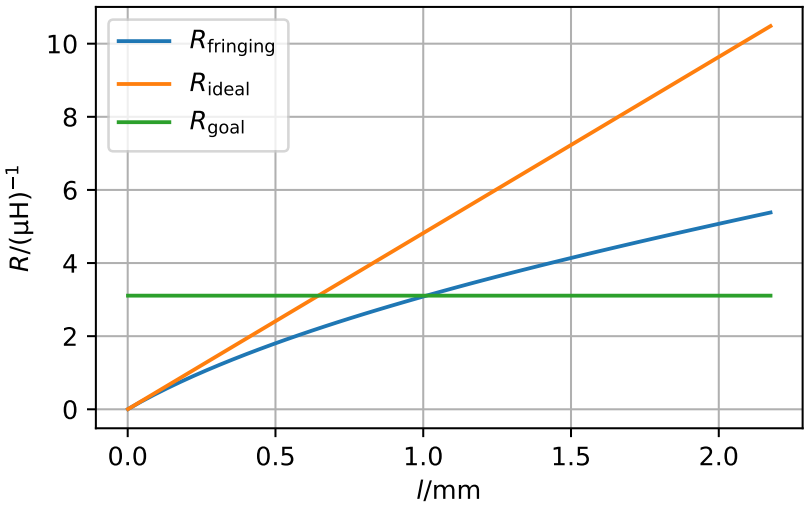

Figure 3.19.: Example resistance calculation for a single air gap: Including fringing fields vs. idealized/linear

figure 3.18) such as "PQ-" or "ETD-"cores to

$$R_{\text{inc.-cyl, ideal}} = \frac{\ln \frac{r_o}{r_o - l}}{\mu_0 \left[2\pi - 4 \arccos \frac{w_{real}}{2r_o}\right]}.[6] \tag{3.37}$$

The corresponding air gap reluctance value including fringing effects can be calculated analogously to 3.36. Unfortunately these air gap reluctance formulations lead to non-linear functions which require a numerical solver. As the reluctance calculated due to [15], (in the relevant interval) increases strictly monotonically with the air gap length, the difference of the goal and the approximated reluctance leads to a zero crossing in exactly one point (cf. figure 3.19). With increasing air gap length, the idealized calculated magnetic resistance deviates more strongly from the approach extended by fringing.

Out of several python given numerical solvers, Brent's method is capable of detecting a function's zero on an interval [16]. Therefore, FEMMT uses the "scipy.optimize.brentq" solver, implemented in the "scipy" toolbox [17]. The solver takes three arguments, the function, a lower and an upper bound of the sign changing interval. Due to *division by*

zero error, the lower bound can always be chosen to a small value below a practically realizable air gap length (for example 1 nm). The upper value can be chosen as the maximal allowed air gap length, which is practically defined by the core's leg length in which the air gap must be placed.

3.7. Minimal Example of FEMMT

To show the basic functionality of the FEM Magnetic Toolbox, a minimal code example is presented in listing 3.2. In this example, a 2D axisymmetric FEM simulation for a coil is proceeded.

```
from femmt import MagneticComponent

geo = MagneticComponent(component_type="inductor")

geo.core.update(type="EI", core_w=0.02, window_h=0.02, window_w=0.012)

geo.air_gaps.update(method="percent", n_air_gaps=3, air_gap_h=[0.001,
    0.0005, 0.001], position_tag=[0, 0, 0], air_gap_position=[10, 50, 90])

geo.update_conductors(n_turns=[[30]], conductor_type=["litz"],
    conductor_radii=[0.0010], strand_radii=[70e-6], ff=[0.6],
    litz_para_type=["implicit_strands_number"], winding=["primary"], scheme
    =["hexa"], core_cond_isolation=[0.002], cond_cond_isolation=[0.0001])

geo.single_simulation(freq=250000, current=[5])
```

Listing 3.2: Minimal Example

A core is defined according to its center core width *core_w*, the winding window height *window_h* and width *window_w*. To avoid saturation and simultaneously reduce the winding losses, caused by proximity effect, a distributed air gap is placed in the middle leg. The winding is defined with 30 turns automatically placed in a hexagonal winding scheme. The conductor type is defined as a litz wire with 70 µm strands. Finally, the

frequency domain simulation is initialized at with a peak current of 5 A.

The simulation results can optionally be viewed in the GUI of GMSH (cf. figure 3.20). The GUI is capable of creating user defined post processing views with mixed field solutions. Further, the mesh can be investigated for certain inaccuracies.

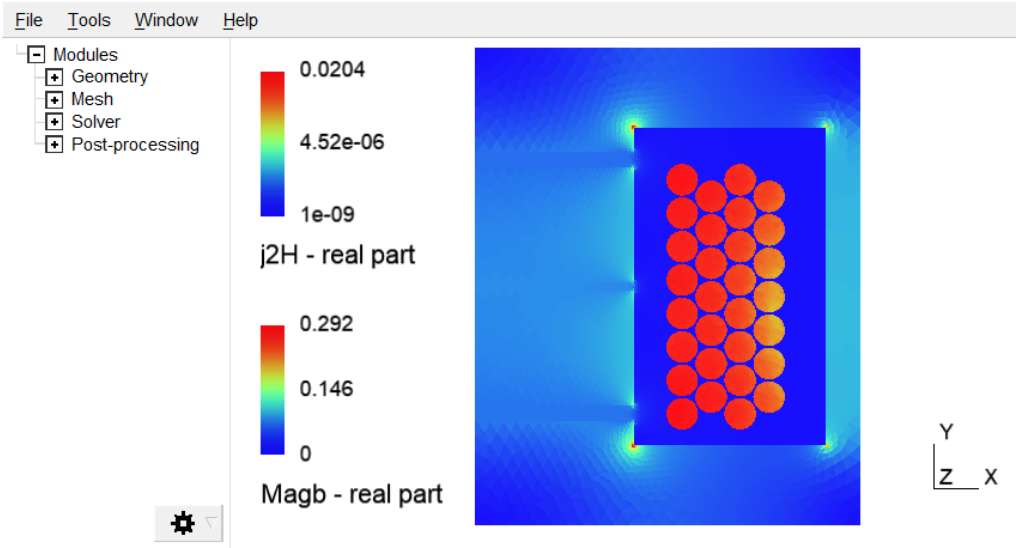

Figure 3.20.: Visualization of the simulation results according to the minimal example from listing 3.2 in the GMSH GUI

4. Design of an Integrated Transfomer for a Dual Active Bridge

The presented FEM toolbox from chapter 3 is used to design an integrated transformer for a Dual Active Bridge DAB converter in an Uninterruptible Power Supply UPS. The UPS under investigation is provided with a bidirectional converter in such way, that power can be fed back into the mains from the battery (cf. figure 1.1). This enables the possibility to contribute to a smart grid by peak shaving or providing frequency containment reserve.

The DAB is specified for an input voltage of 700 V DC, an output/battery voltage of 216 V DC and 34 kW nominal output power. In this thesis a laboratory prototype with nominal power $P_{\mathrm{nom}} = 2\,\mathrm{kW}$ and overload reserve of 25 % ($P_{\mathrm{max}} = 2.5\,\mathrm{kW}$) is to be designed and tested. The laboratory prototype must provide the maximal power for an output voltage range of 175 V to 295 V.

The circuit diagram of a DAB is presented in figure 4.1. Herein, V_{ib} and i_{ib} respectively

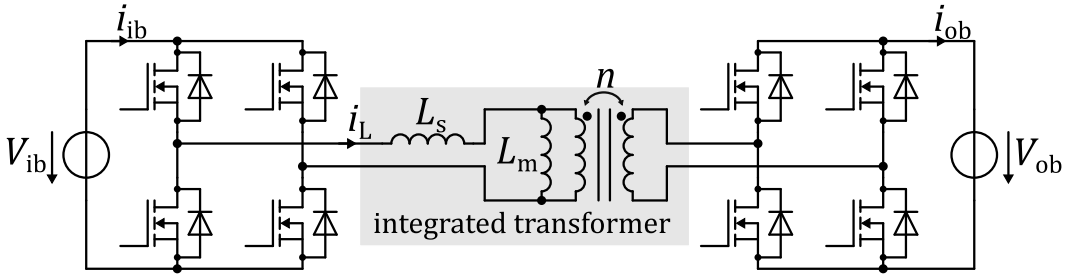

Figure 4.1.: DAB converter with transformer and circuit parameters

Table 4.1.: Influence of the mutual inductance L_m on the semiconductor losses at a fixed stray inductance $L_\mathrm{s} = 85\,\mu\mathrm{H}$.

L_m	inf	10 mH	850 µH(= $10L_\mathrm{s}$)	400 µH	100 µH
I_L/A	3.9	3.9	3.9	3.9	4.0
I_ib/A	2.8	2.8	2.8	2.9	3.0
I_ob/A	8.8	8.8	9.0	9.2	13.1
$\overline{p_\mathrm{sw,\,ib}}$/W	2.2	2.2	2.2	2.2	2.2
$\overline{p_\mathrm{cond,\,ib}}$/W	1.4	1.4	1.4	1.5	1.6
$\overline{p_\mathrm{tot,\,ib}}$/W	3.6	3.6	3.6	3.7	3.8
$\overline{p_\mathrm{sw,\,ob}}$/W	0.6	0.6	0.8	1.1	3.1
$\overline{p_\mathrm{cond,\,ob}}$/W	12.6	12.6	12.9	13.8	29.2
$\overline{p_\mathrm{tot,\,ob}}$/W	13.2	13.2	13.7	14.9	32.2

V_ob and i_ob are introduced as the voltage and current of the input bridge IB and output bridge OB. To enable zero voltage switching (ZVS), a significant stray inductance L_s is needed. This can either be realized by a discrete transformer and choke or in one component with an integrated transformer. As the stray inductance may be chosen anti-proportional to the switching frequency f_sw, the design parameter

$$\lambda = L_\mathrm{s} f_\mathrm{sw} \tag{4.1}$$

is introduced. Based on a fixed λ, it is possible to set a goal stray inductance depending on the switching frequency. Unlike the design of a resonant converter, the main inductance L_m must not meet an exact value to achieve a certain resonant frequency. Nevertheless, circuit simulations show, that a high value of L_m is desirable. This statement can be quantified by considering the semiconductor losses. According to circuit design simulations [18], the semiconductor losses are estimated depending on the inductance ratio $L_\mathrm{m}/L_\mathrm{s}$. The average losses are distributed among the IB and OB with $\overline{p_\mathrm{tot,\,ib}}$ and $\overline{p_\mathrm{tot,\,ob}}$. Both total losses are in each case the sum of the switching and conduction losses $\overline{p_\mathrm{sw}}$ and $\overline{p_\mathrm{cond}}$ of all four semiconductors of the input and output bridge.

According to table 4.1, particularly the RMS current I_ob of the output bridge strongly increases with decreasing main inductance. For a simple visualization all critical values

in table 4.1 are marked as orange and bad values as red. For values marked as green, almost no influence of the mutual inductance on the losses can be observed. From here, a practical design goal for this application can be derived to aim for a $L_{\mathrm{m}} \approx 10 \cdot L_{\mathrm{s}}$. The goal parameters are completed with the transformer ratio n, which in turn is chosen according to circuit simulations [18].

In this thesis, no further coupling of the magnetic component and electrical circuit design is implemented. To optimize the transformer regarding its efficiency, it is searched for the geometric design with the lowest losses in a limited volume. The optimization problem is constrained by the three goal parameters L_s, L_m and n. Further, saturation limits the maximum magnetic flux density in the core. Thus, the maximum magnetic flux density be seen as a restriction caused by material properties.

4.1. Component Modelling

A parameterized model is essential for an automated design process of a magnetic component. The disadvantage of a complete parameterization is the enormous complexity. To shrink the parameter space a priori, some constraints are taken into account.

- Air gaps are only modelled in the center leg of the core. Due to this restriction, the Electromagnetic Interference (EMI) for the transformer's immediate surroundings is reduced [6]. Further, for a 2D axisymmetric simulation, the boundary condition of the magnetic vector potential can directly be placed on the core itself.
- A dedicated stray path is always assumed.
- Only stranded conductors are taken into account to reduce the winding losses.

4.1.1. 2D Axisymmetric Approximation

An integrated transformer in the 2D axisymmetric simplification (cf. figure 3.1) can be parameterized according to figure 4.2. Only the three parameters w_{core}, h_{window} and w_{window} describe the main core. For this thesis, an N95 PQ 40/40 core from TDK Electronics is used as the basis core [19]. Due to that, the three main core parameters are fixed by the given specification. At this point, it should be mentioned, that FEMMT is capable of sweeping any geometrical parameters, including the core parameters. The decision to use a standard core early in the design process enables a faster and easier manufacturing process.

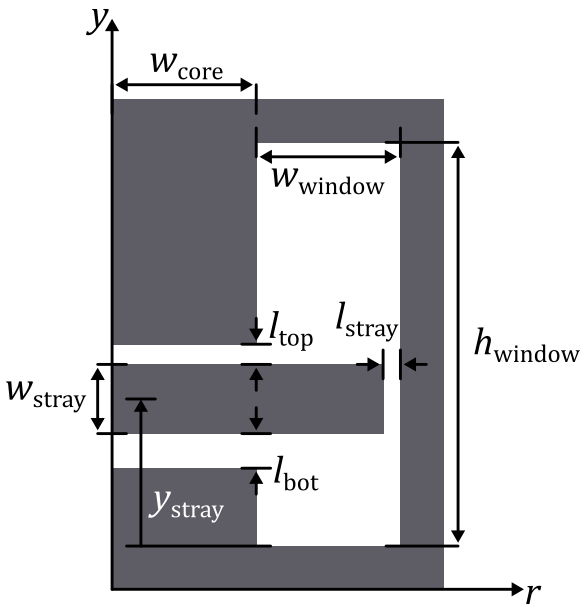

Figure 4.2.: Parametrization of an axial symmetrical integrated transformer

The dedicated stray path can be described by two parameters. First, the vertical position y_{stray} of the stray path relative to the window height can be expressed with

$$y_{\text{stray, rel}} = \frac{y_{\text{stray}}}{h_{\text{window}}}. \tag{4.2}$$

For an optimization of a core with fixed dimensions, this approach does not enable

any benefits. But assuming also a parameter sweep of the core height, the relative positioning in accordance to the window height helps to avoid the definition unrealistic parameters, such as vertical positions higher than the window itsself.

Second, the stray path width w_{stray}, is set in relation to the occurring magnetic flux density. According to that, the flux density ratio ζ_{stray} is introduced with

$$\zeta_{\text{stray}} = \frac{b_{\text{stray}}}{\max(b_{\text{top}}, b_{\text{bot}})}. \tag{4.3}$$

The flux density ratio couples magnetic flux densities in the top and bottom leg to describe the stray path width. This is useful, because a very low magnetic flux density leads to an oversizing of the stray path, while a very high magnetic flux density leads to an undersizing corresponding to local saturation.

Both stray path parameters, the vertical position and flux density ratio, are set in relation to other core parameters. This coupling of parameters helps the user to define the parameter space more precisely than just defining arbitrary lists of values.

Beyond the core, windings must be configured. According to the reluctance model of an integrated transformer (cf. figure 3.14) the four parameters N_{11}, N_{12}, N_{21} and N_{22} describe the numbers of turns in the two winding windows. Differently to the reluctance model, for FEM simulations the exact positioning of the conductors needs to be defined. For this purpose, FEMMT is capable of defining some winding schemes according to input parameters.

In this thesis it is decided to use horizontal interleaving as the winding scheme. This means that primary and secondary windings are alternately wound around the bobbin (barrel windings). This is a compromise that matches a simple manufacturing process of the transformer while reducing the proximity effect. According to [1], a bifilar winding scheme is most advantageous in terms of reducing the proximity effect. But especially for a transformer ratio strongly deviating from 1, the manufacturing effort is comparatively high.

4.1.2. Initial Grid Search Parametrization

The most simple way of finding an optimum in a feature space, is the brute force approach of trying out any possible parameter vector. An initial parameter grid $\mathbb{S}^{\text{init}}$ for an N^{init} dimensional feature space is given with

$$\mathbb{S}^{\text{init}} = \{\boldsymbol{p}_{\text{init}}(1), ..., \boldsymbol{p}_{\text{init}}(n), ..., \boldsymbol{p}_{\text{init}}(N^{\text{init}})\}. \tag{4.4}$$

Herein, the n^{th} M dimensional parameter vector $\boldsymbol{p}_{\text{init}}(n)$ is defined as

$$\boldsymbol{p}^{\text{init}}(n) = \begin{bmatrix} p_1(n) \\ p_2(n) \\ ... \\ p_m(n) \\ ... \\ p_M(n) \end{bmatrix}. \tag{4.5}$$

For continuous parameters, the number of possible parameter vectors is infinite and must be discretized. For discrete parameters, such as the numbers of turns in the winding windows, only the range has to be defined.

An initial parameter set for the integrated transformer is presented in table 4.2. All combinations of the geometrical parameters lead to 50544 possible parameter vectors. For a complete illustration, the switching frequency f_{sw} is already listed at this point and leads to a total number of 252720 possible parameter vectors.

4.1.3. Motivation for an Analytical Reluctance Model

Describing a 2D axisymmetric core, windings and materials via parameters leads to some hundred thousand parameters, even for a quite coarse grid search (cf. table 4.2). Herein, different materials, main cores, winding schemes and litzes are even not taken into

Table 4.2.: Initial parameter set $\mathbb{S}^{\text{init}}$ for a grid based optimization

	min	**max**	**no. parameters**
N_{11}	18	29	12
N_{12}	4	9	6
N_{21}	0	12	13
N_{22}	0	8	9
$\text{y}_{\text{stray, rel}}$	30 %	40 %	3
ζ_{stray}	100 %	150 %	2
f_{sw}	200 kHz	300 kHz	5

account. Modelling a complete three dimensional geometry of course would even lead to much more parameters. By investigating the complexity of this modelling problem, a grid search involves 50544 geometrical parameters at 5 frequencies. Assuming a computation time of 20 s per parameter FEM simulation (on a standard laptop) leads to a total computation time of 58.5 days. In this calculation, it is assumed, that the corresponding air gap lengths are somehow known a priory. The main problem is, that for such a wide parameter space, most of the configurations are either not realizable in a geometric sense or they lead to very deviating inductance values from what is the design goal.

One solution to this problem is the usage of a precise analytical reluctance model, such as presented in section 3.6.2. This model can predict the air gap lengths and determine whether the core (or a part of it) is saturated. The reluctance model is initialized with core dimensions, winding numbers and the goal inductance matrix as input parameters. Depending on the chosen type of magnetic component (coil, transformer or integrated transformer) a magnetic equivalent circuit individually is set up.

4.2. Transformer Behaviour of a Dual Active Bridge Converter

The idealized behaviour of the transformer in the underlying DAB typology is investigated according to the reluctance model presented in section 3.6.2. For this purpose, currents and fluxes are illustrated for two working points with maximal power and min-

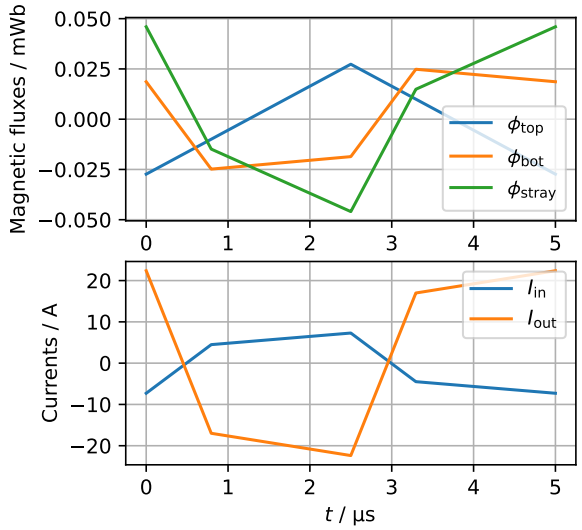

(a) Current and flux waveforms for the working point with the maximal current ($P_{out} = P_{max} = 2.5\,kW$ and $V_{out} = 175\,V$)

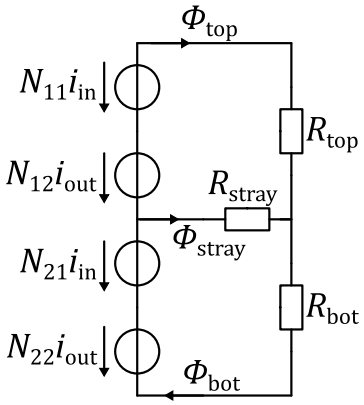

(b) Magnetic ECD

Figure 4.3.: Waveforms and magnetic ECD for the integrated transformer (cf. section 3.6.2)

imum voltage and with nominal power and nominal voltage. The first working point is used to supervise the saturation of the ferrite, whereas the second is used for the transformer optimization in terms of efficiency maximization.

4.2.1. Analytical Check of Saturation

To check for possible saturation in any part of the ferrite core, the magnetic flux corresponding to the underlying current waveforms in the working point with maximum current and minimum output voltage (at $P_{max} = 1.25 \cdot P_{nom}$) are investigated (cf. figure 4.3(a)). For this working point, it can be concluded, that the largest flux peak occurs in the stray path.

To control whether the core is saturated or not, the locally averaged flux densities in the bottleneck of each leg are determined and checked according to the fluxes in

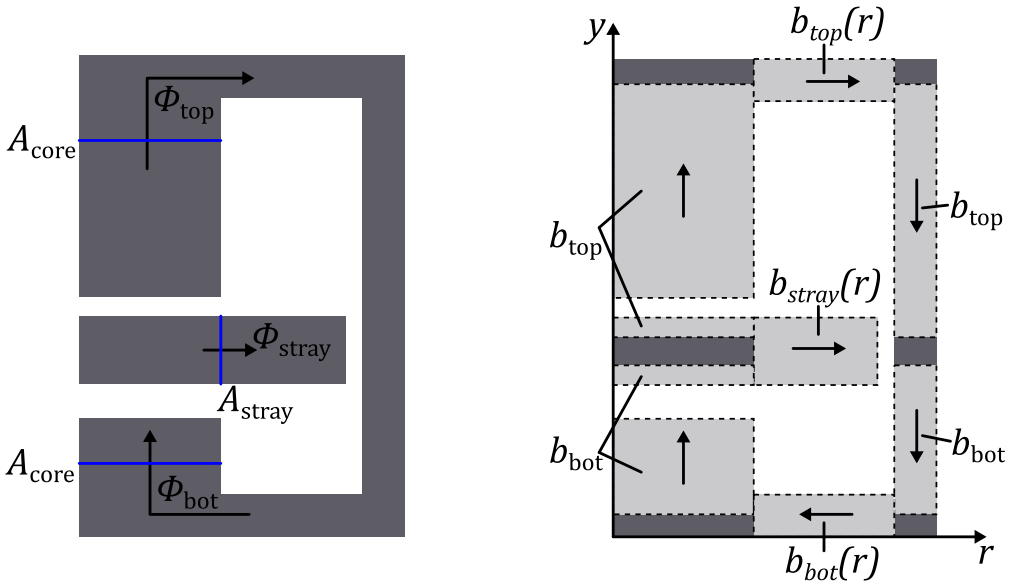

(a) "Bottleneck" surfaces to check for saturation

(b) Core parts for the piece wise calculation of magnetic flux densities for hysteresis loss estimation

Figure 4.4.: Analytical evaluation of the integrated transformer

figure 4.3(a). The maximum locally averaged flux densities in the top and bottom leg are simply defined by the surface area A_{core} of the middle leg (cf. figure 4.4(a)). For the stray path, this bottleneck is defined by the cylindrical surface area A_{stray} with the diameter of the middle leg and the height of the stray path tablet (cf. figure 4.4(a)).

4.2.2. Analytical Estimation of Hysteresis Losses

By recapturing the hysteresis loss calculation with complex material parameters (cf. section 3.5.1), it can be stated, that a local (FEM) frequency domain approximation only makes sense, if the original time domain flux wave form can be represented in good approximation by a sinusoidal current excitation.

For this DAB application with an integrated transformer, the flux waveforms, according to fundamental current excitation, do not correspond to the time domain flux

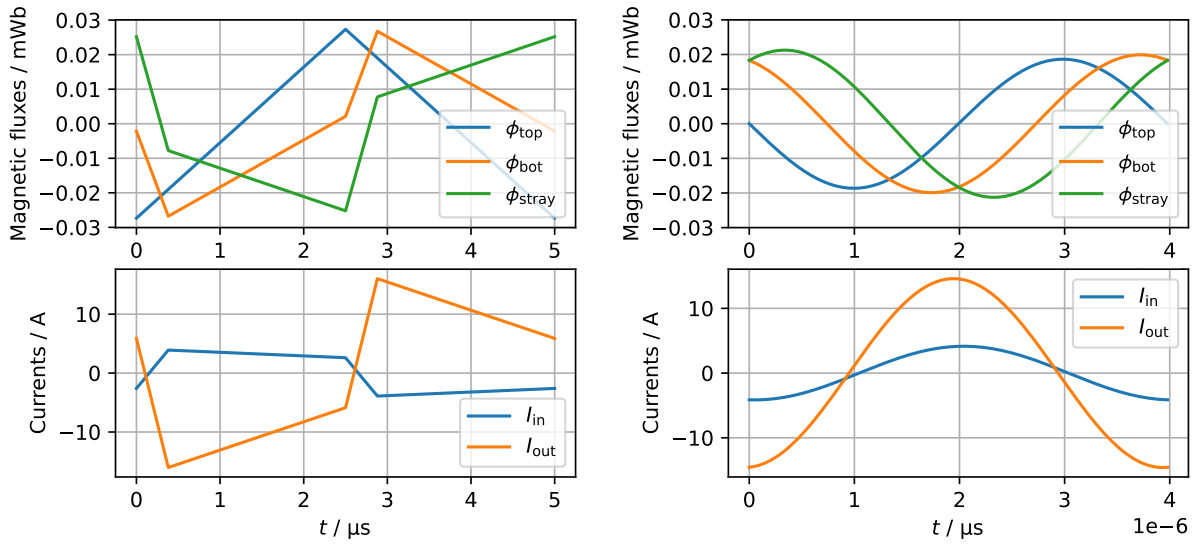

(a) Time Domain

(b) Fundamental Content

Figure 4.5.: Current and flux waveforms for the working point with nominal power and nominal voltage ($P_{out} = P_{nom} = 2\,\mathrm{kW}$ and $V_{out} = 235\,\mathrm{V}$)

waveforms (cf. figure 4.5). The problem with the fundamental current excitation for such a branched inductive component is, that the resulting peak fluxes in the single core parts strongly differ from the time domain results. As the peak magnetic flux density B_{max} is mostly relevant for hysteresis losses, a loss estimation based on figure 4.5(b) is unacceptable. This is why a frequency domain based FEM based approach to calculate the hysteresis losses can be discarded.

Alternatively, the reluctance model is used, to calculate the maximum fluxes in each leg from the time domain currents according to figure 4.5(a). The resulting peak values from the time domain approach are treated as sinusoidal fluxes (cf. figure 4.6) and transferred to formula 3.20. For this purpose, the three magnetic fluxes ϕ_{top}, ϕ_{bot} and ϕ_{stray} need to be transformed into corresponding local absolute values of complex RMS magnetic field pointers $|\underline{\boldsymbol{H}}|$ according to

$$|\underline{\boldsymbol{H}}| = \frac{\max_t(|b|(t))}{\sqrt{2}\mu_0\mu_r}. \tag{4.6}$$

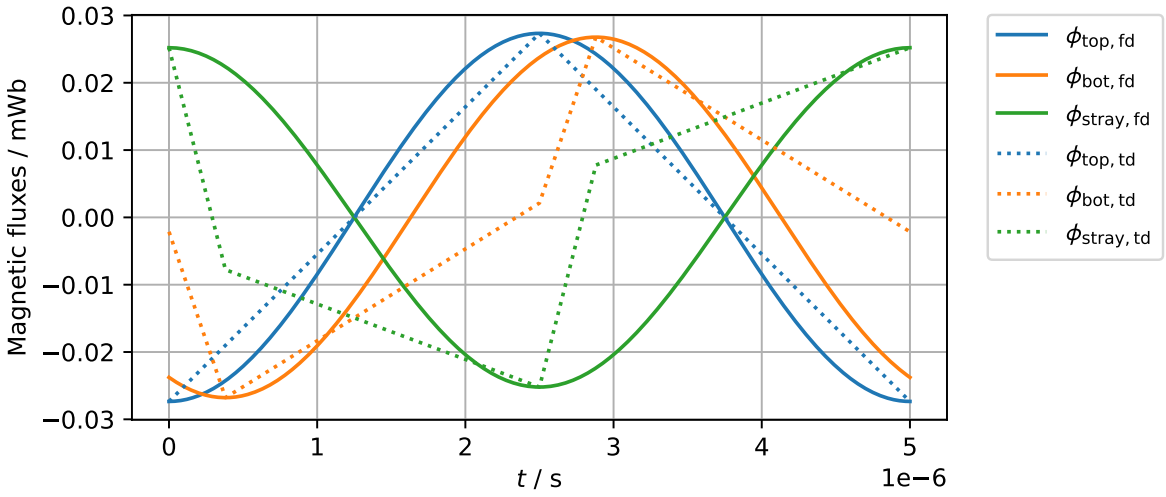

Figure 4.6.: Frequency domain (fd) approximation of the time domain (td) fluxes occurring in the three core parts

This leads to an adjusted formula 3.20, which represents the analytical hysteresis loss density as

$$p_{a.hyst} = -\frac{1}{2}\omega\Im(\underline{\mu})\left(\frac{\max_t(|b|(t))}{\mu_0\mu_r}\right)^2. \tag{4.7}$$

Herein, $\max_t(|b|(t))$ denotes the maximum of the time dependent absolute magnetic flux density.

To calculate the hysteresis losses for a certain core, the geometry can be split into regions, where it is possible to describe the magnetic flux density piece wise according to figure 4.4(b). For the core parts with flux density vectors parallel to the y-axis, b_{top} and b_{bot} have constant values. For these regions the hysteresis loss density according to formula 4.7 can simply be multiplied with the region's volume. For the core parts orthogonal to the y-axis, the magnetic flux density depends on the radial coordinate r, yielding $b_{\text{top}}(r)$, $b_{\text{bot}}(r)$, and $b_{\text{stray}}(r)$. Due to that, the hysteresis loss density according to formula 4.7 also depends on r and thus an integration over the corresponding core volume is needed. In the python implementation, the numerical integration is performed

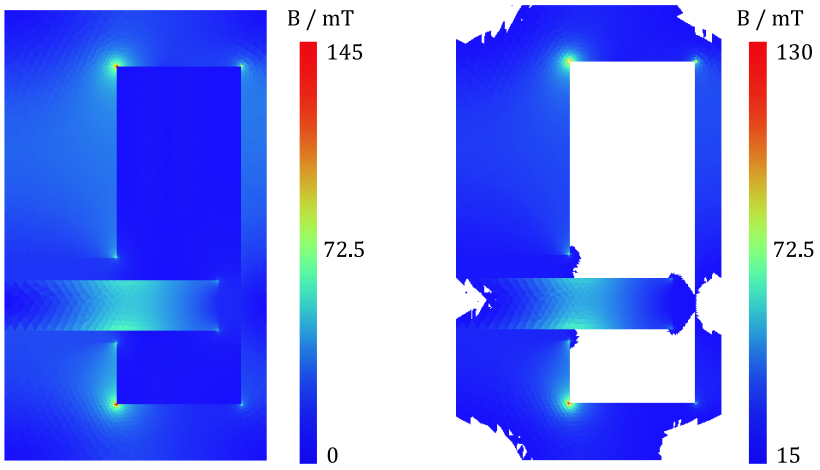

(a) Full scale (b) Between 10 and 90 %

Figure 4.7.: Exemplary distribution of the magnetic flux density B for an integrated transformer)

with the "quad" integrator form the "scipy.integrate" package [20].

The choice of the piece wise core regions in figure 4.4(b) is carried out according to the resulting magnetic flux distribution of a FEM simulation. From such a flux density visualization (cf. figure 4.7(b)), it can be observed that the magnetic flux is concentrated in the inner corners of each path. For simplicity, the volume for hysteresis losses is modeled by simple blocks, assuming that each corner is used with half of its volume. This approach can be extended in future by involving fringing effects analog to section 3.6.3. As figure 4.4(b) shows, the air gaps are excluded from the volume.

To cross validate the developed analytical hysteresis loss model with the FEM based approach, derived in section 3.5.1, the results of a simulation for a purely sinusoidal current excitation (cf. "harmonic excitation" in figure 4.8) are investigated. For this purpose, in total 67 different parametrizations of integrated transformer topologies are simulated and the hysteresis losses according to the three approaches are plotted. The comparison for a pure harmonic current excitation shows, that the analytical model under-predicts the hysteresis losses compared to the FEM based approach with a mean deviation normalized on the FEM based results of 8.7 %. This may be explained due

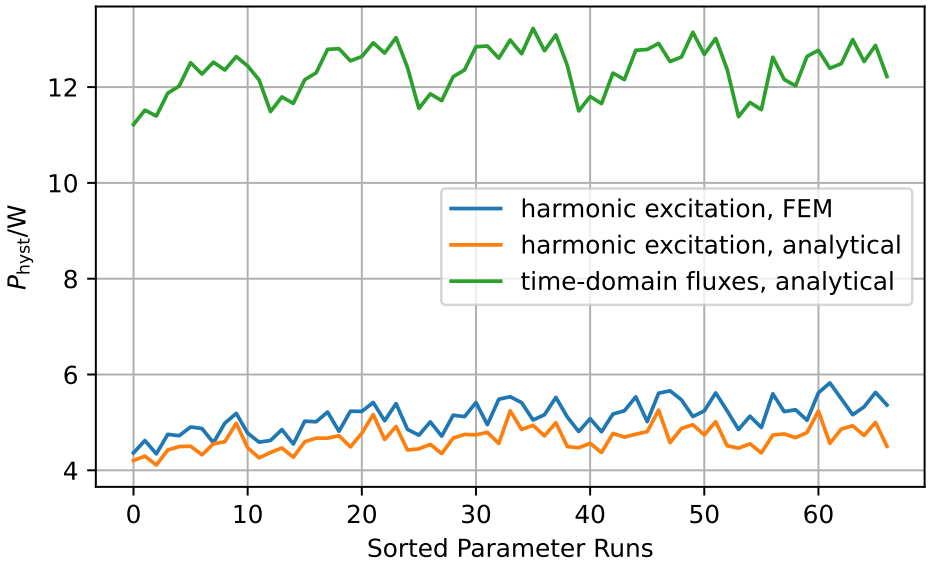

Figure 4.8.: Comparison of the estimated hysteresis losses according to the presented approaches in a typical integrated transformer application (all three approaches are calculated in FEMMT)

to the assumption of homogenized fields in the reluctance model, which is used for the analytical approach, whereas FEM simulations show a flux concentration in the inner corners of the core (cf. figure 4.7(a)). Due to the very fast and simplified loss calculation in the analytical model, the deviation is acceptable.

For the optimization, the analytical approach is combined with time-domain estimated flux peaks. This approach clearly exceeds the approaches with harmonic excitation (cf. figure 4.8, "time-domain fluxes, analytical").

An advantage of an analytical calculation of hysteresis losses is, that it can be performed before the FEM simulation. This enables the prefixed exclusion of parameter sets subjected to high losses. For future works, the complex core parameters may also be measured at non sinusoidal currents. This is not concerned in this work.

4.3. Optimization of the Geometry

The integrated transformer model according to section 4.1 is to be optimized according its efficiency. The optimization is constrained to avoid saturation and provide the required circuit parameters according to the given electrical simulations. The efficiency is optimized in the working point with nominal voltage and nominal power. Another possible target parameter of the optimization is the power density. But, due to the restriction of using a PQ 40/40 core, the transformer's volume is more or less fixed except of the outstanding windings. Finally, the result of this optimization is chosen to be the geometric parametrization with the lowest total losses.

The optimization procedure is initialized with the initial parameter set $\mathbb{S}^{\text{init}}$ according to table 4.2, which corresponds to the "global grid" in the exemplary optimization routine for a two dimensional feature space according to figure 4.9. This initial grid search is characterized by a coarse parameter grid with increments Δ^{init}. At the end of this initial run, a first global optimum opt_1 is obtained based on the coarse initial grid.

After the this global grid search follows a local optimization routine. By iteratively initializing local grids with increments $\Delta^{\text{local}}(\leq \Delta^{\text{init}})$ around the last iteration's optimum, it can be possible to locate new parameter vectors with lower total losses. This procedure is repeated until no new optimum is found. In the abstract example of figure 4.9, the optimization algorithm converges after three local iterations, as it holds $opt_4 = opt_3$.

An exemplary local grid $\mathbb{S}^{\text{local}}$ is defined as a set of N^{local} parameter vectors $\boldsymbol{p}_{\text{local}}(n)$ with

$$\mathbb{S}^{\text{local}} = \{\boldsymbol{p}_{\text{local}}(1), ..., \boldsymbol{p}_{\text{local}}(n), ..., \boldsymbol{p}_{\text{local}}(N^{\text{local}})\}. \tag{4.8}$$

The parameter vectors of the local grid are calculated around the last iteration's

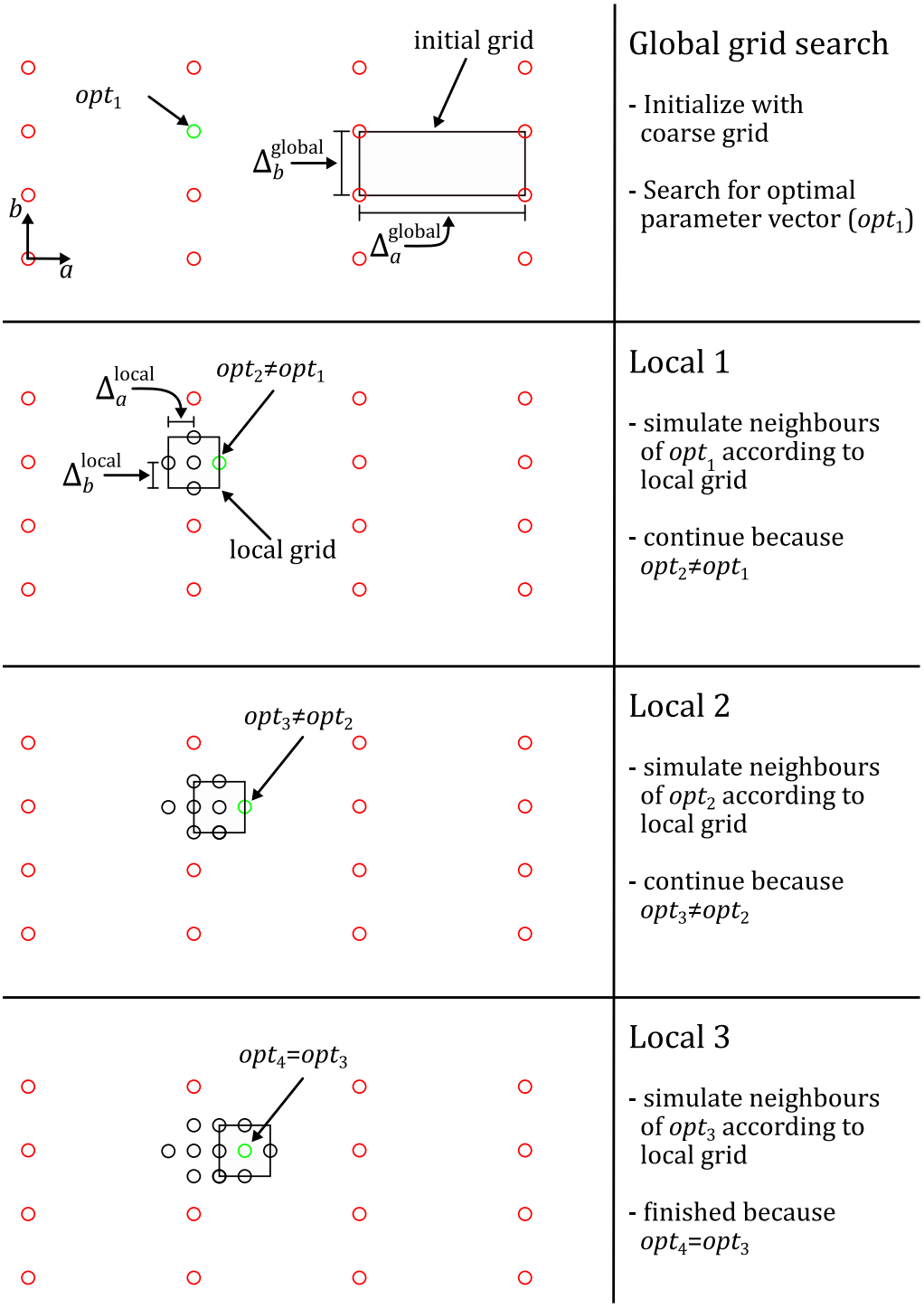

Figure 4.9.: Abstract example of the implemented optimization routine for a two-dimensional feature space

optimum $\boldsymbol{p}_{\text{opt}}$ with relative update parameter vectors $\boldsymbol{p}_{\text{update}}(n)$ as

$$\boldsymbol{p}_{\text{local}}(n) = \boldsymbol{p}_{\text{opt}} + \boldsymbol{p}_{\text{update}}(n). \tag{4.9}$$

The n^{th} update parameter vector is given as

$$\boldsymbol{p}_{\text{update}}(n) = \begin{bmatrix} u_1 \in \mathbb{U}_1 \\ u_2 \in \mathbb{U}_2 \\ \dots \\ u_m \in \mathbb{U}_m \\ \dots \\ u_M \in \mathbb{U}_M \end{bmatrix}. \tag{4.10}$$

Herein, the set $\mathbb{U}_m$ denotes the local grid for the m^{th} parameter with the local grid increment Δ_m^{local} and the number of grid steps s_m as

$$\mathbb{U}_m = \{-s_m\Delta_m^{\text{local}}, \dots, -2\Delta_m^{\text{local}}, -\Delta_m^{\text{local}}, 0, \Delta_m^{\text{local}}, 2\Delta_m^{\text{local}}, \dots, s_m\Delta_m^{\text{local}}\}. \tag{4.11}$$

Each set contains a zero/neutral element, that doesn't have any effect on the new parameter vector. The remaining elements describe the positive and negative incrementation of the parameter according to the chosen local grid increment.

For the local optimization of the integrated transformer for a DAB, the updates of the winding matrix' elements U_N, the relative stray path position $y_{\text{stray, rel}}$ and the relative stray path width ζ_{stray} are chosen as

- $\mathbb{U}_N = \{-3, -2, -1, 0, 1, 2, 3\}$
- $\mathbb{U}_y = \{-1\,\%, 0\,\%, 1\,\%\}$
- $\mathbb{U}_\zeta = \{-10\,\%, 0\,\%, 10\,\%\}$.

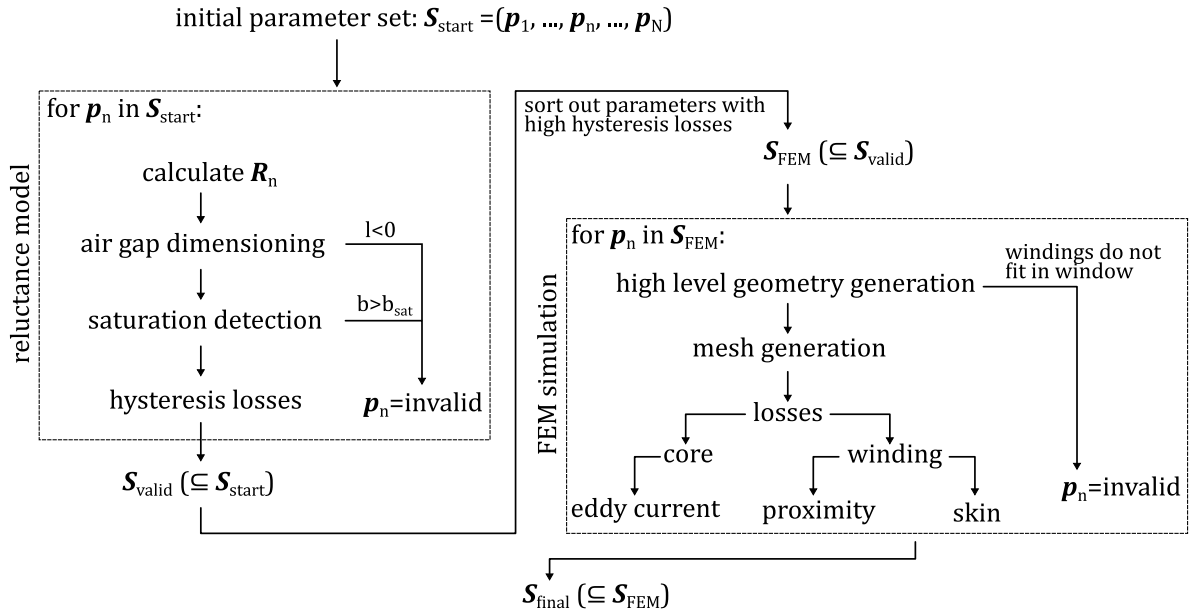

Figure 4.10.: Workflow of a grid search run initialized with the parameter set $\boldsymbol{S}_{\text{start}}$

4.3.1. Grid Search: Workflow of a Parameter Set

Each run in figure 4.9 is carried out according to the same workflow, no matter it is the initial or a local run. The only difference is the intial parameter set, which defines the grid on which an optimum is searched. A parameter set $\boldsymbol{S}_{\text{start}}$ with $N = |\boldsymbol{S}_{\text{start}}|$ feature vectors is assumed to initialize the calculation routine shown in figure 4.10. (The notation is switched from sets (blackboard bold) to matrices (bold), to indicate that parameter sets in the python code of FEMMT are defined as lists of dictionaries, compactly stored in *numpy* arrays.

According to section 3.6.2 the reluctance model is used for prefixed calculations in a loop for every parameter vector $\boldsymbol{p}_{\text{n}} \in \boldsymbol{S}_{\text{start}}$. First the reluctance matrix $\boldsymbol{R}_{\text{n}}$ is calculated from the goal inductance matrix $\boldsymbol{L}$ and the parameter vector's winding matrix $\boldsymbol{N}_{\text{n}}$. Further, the air gap lengths are dimensioned including fringing effects according to section 3.6.3. Subsequently, each leg of the ferrite core is checked for saturation. If any of the calculated air gap lengths is negative or in case the magnetic flux density exceeds the saturation limit, the parameter vector $\boldsymbol{p}_{\text{n}}$ is labeled as invalid. Finally, in

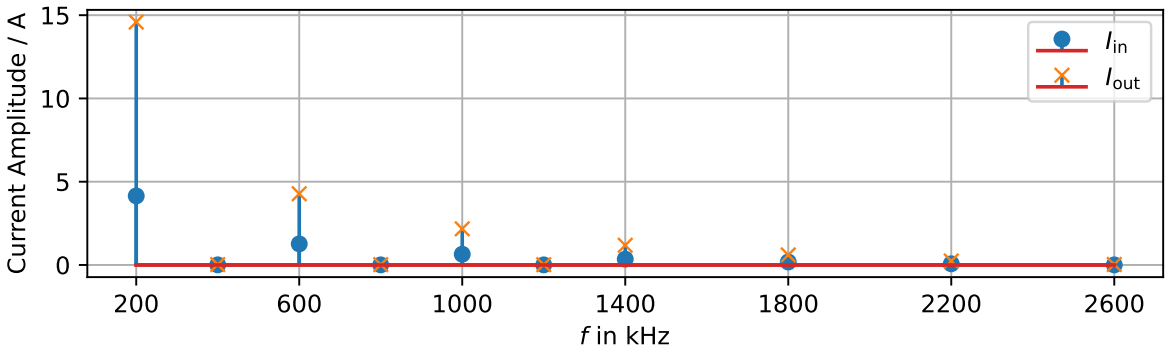

Figure 4.11.: Current amplitudes according to the frequency spectrum of the current wave forms in the working point with nominal output voltage and nominal output power (cf. figure 4.5(a))

the reluctance model, for the valid parameter set $\boldsymbol{S}_{\text{valid}}$ the analytical hysteresis losses are calculated according to section 4.2.2.

Before initializing the FEM simulations, all parameter vectors that exceed the minimum's hysteresis losses by more than a certain factor (for example 150 %) are sorted out of the parameter set. Since the hysteresis losses account for the majority of the losses, these parameter vectors are no promising candidates for the final optimum.

In the FEM simulation, all geometrically impossible configurations are sorted out of the FEM parameter set $\boldsymbol{S}_{\text{FEM}}$. Further, the losses according to eddy currents in the core as well as proximity and skin effect in the windings are calculated. For these frequency domain simulations, only the current-phase pairs for the frequencies with a significant current amplitude are considered. For that purpose, it is possible to sort out all frequencies with an amplitude smaller than a certain factor relative to the maximum amplitude (for example 5 %). For the DAB, it is sufficient to perform FEM simulations for the four dominating frequencies (cf. figure 4.11). The FEM simulations are accelerated by not calculating single field quantities, but only solving the FEM system equation and then directly extracting the loss values by integration. Further, the mesh is only created once for every parameter vector and then reused in every single simulation. The output of the iterative FEM simulations is the final parameter set $\boldsymbol{S}_{\text{final}}$, which easily can be investigated to find the loss optimum.

Table 4.3.: Parameter statistics of the optimization procedure

Run	**Frequency**	$\lvert \boldsymbol{S}_{\text{start}} \rvert$	$\lvert \boldsymbol{S}_{\text{valid}} \rvert$	$\lvert \boldsymbol{S}_{\text{FEM}} \rvert$	$\lvert \boldsymbol{S}_{\text{final}} \rvert$
Global 1	200 kHz	50544	3435	603	12
Global 2	225 kHz	50544	5073	838	13
Global 3	250 kHz	50544	6426	901	14
Global 4	275 kHz	50544	7473	919	14
Global 5	300 kHz	50544	8388	927	14
Local 1	200 kHz	12348	1758	823	48

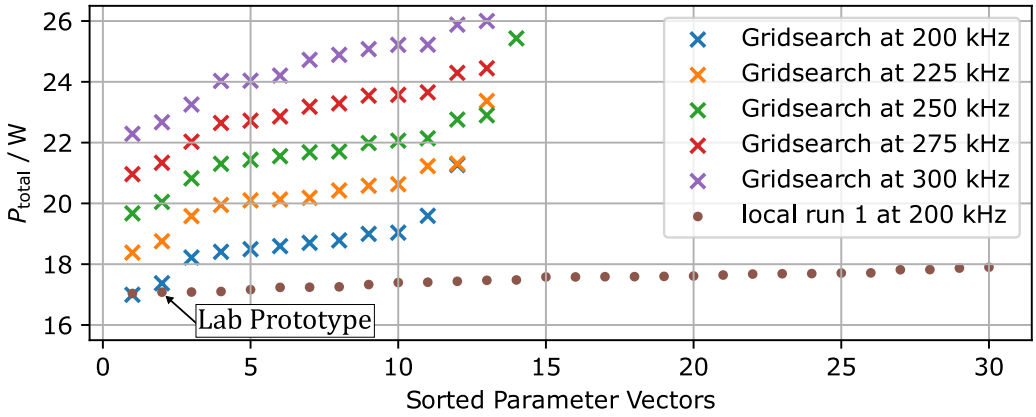

Figure 4.12.: Total losses of the final parameter set $\boldsymbol{S}_{\text{final}}$ (cf. figure 4.10) within the optimization procedure (Data is adjusted for outliers; for raw plot cf. figure B.1)

4.3.2. Optimization Results

The grid search is initialized with the parametrization, defined in section 4.1, consisting of 50544 geometric parameters for each working point frequency (cf. "Global 1-5", table 4.3). According to table 4.3, the number of valid parameters is reduced in each sub step of the execution. After finding a global optimum on the initial grid, the local simulation is initialized with 12348 parameter vectors according to the updates $\mathbb{U}_N$, $\mathbb{U}_y$ and $\mathbb{U}_\zeta$. Herein, parameter vectors that overlap with the previous grid or with unrealistic parameter values (negative winding numbers) are already excluded.

The total losses of the final parameter sets $\boldsymbol{S}_{\text{final}}$ according to each optimization run

Table 4.4.: Losses of the optimal transformer configuration according to the FEM simulation

P_{core}		P_{winding}		P_{total}
10.34 W		6.74 W		17.08 W
P_{hyst}	P_{eddy}	P_{prim}	P_{sec}	
9.52 W	0.82 W	3.41 W	3.33 W	

are visualized in figure 4.12. The local grid search is performed at 200 kHz, as the previous global grid search clearly shows minimum losses at this switching frequency. In the local run ("Local 1"), 48 valid FEM results are calculated locally "around" the global optimum. As none of the valid results leads to a new optimum regarding the total losses, the local grid search converges after only one iteration.

For the laboratory prototype, the configuration marked in figure 4.12 is chosen. As the simulation results show, there are several candidates with similarly low losses. In addition to the loss values, soft factors also play a certain role in the decision process. Possible reasons are material cost or manufacturing complexity. Since the 2D axisymmetric simulation does not perfectly represent the real world, experience-based considerations can also influence the decision process. For example, considering the stray path as a thermal bottleneck, a designer may choose the parameter vector with the lowest core losses.

The total losses of the chosen parameter configuration for the "Lab Prototype" are estimated with 17.08 W (cf. table 4.4). About 60 % of the losses are allocated to core losses. Herein, the hysteresis losses are clearly dominating with 10.34 W. The winding losses of 6.74 W in total are distributed almost evenly between the primary and secondary sides.

A selection of FEM field solutions is presented in figure 4.13. According to figure 4.13(a) the main winding losses are contributed by the proximity effect due to fringing fields of the air gaps. It can be stated, that this configuration with a very small air gap $R_{\text{top}} \approx 0$ leads to low winding losses in the upper winding window. A further improvement of the winding losses in the lower winding window would be possible by distributing the air gap.

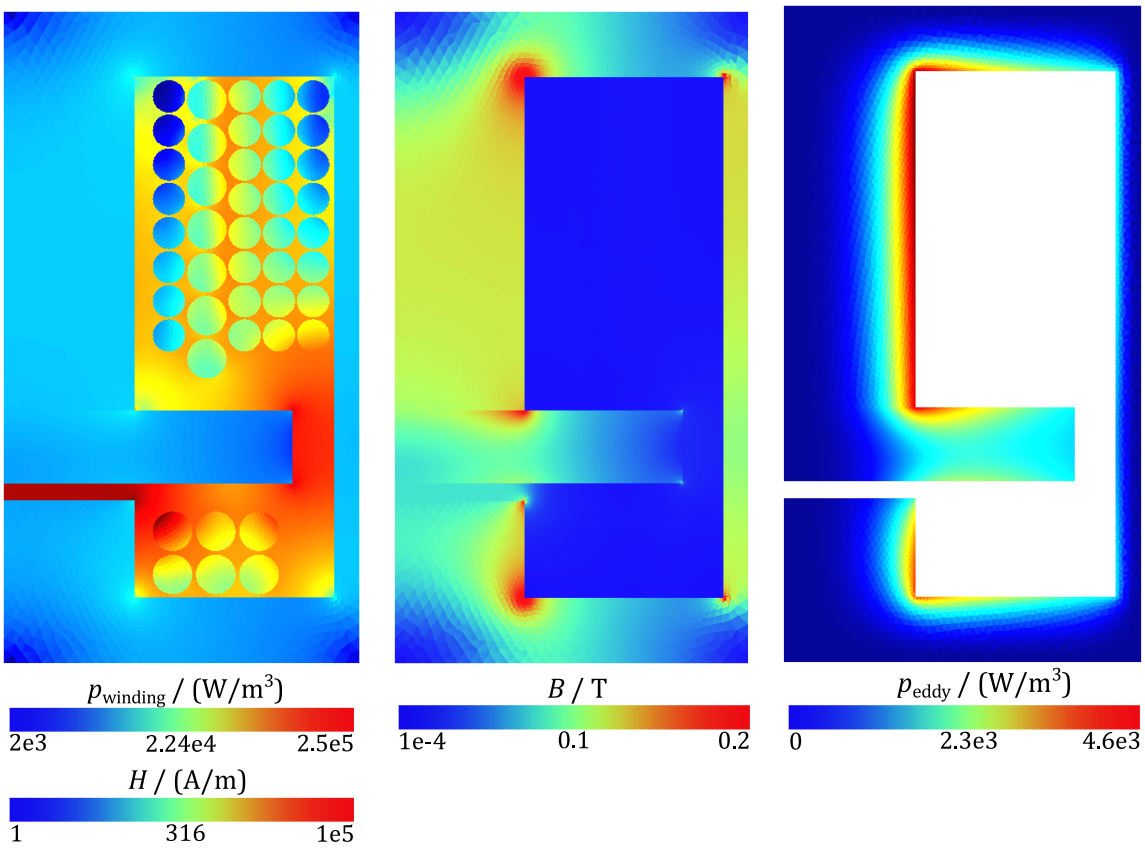

(a) Magnetic Field and Winding Loss Density (b) Magnetic Flux Density (c) Eddy Current Loss Density

Figure 4.13.: FEM simulation results of the optimized transformer; Results for first harmonic of the working point with nominal output voltage and nominal power

The loss density due to eddy current effects p_{eddy} (cf. figure 4.13(c)) shows that the eddy current effects are dominant in the middle leg. Comparing the legend scales of p_{winding} and p_{eddy}, reflects the results from table 4.4, where the eddy current losses are estimated significantly smaller than the winding losses.

4.4. Workflow: Problems and Future Tasks

To fulfil the validation of the presented optimization, besides the quantifiable results, also the workflow is subjected to a critical examination. To this end, the following are some points to reconsider in future developments of the optimization workflow:

- More exact inductance estimation for small air gaps in the analytical reluctance model by including the core's reluctance value
- Implementation of complex core parameters for non sinusoidal fluxes (e.g. trapezoidal, triangular shapes)
- Temperature Model
  - Consideration of material's temperature dependence in core loss model
  - Supervision of overheating
- Involve fringing effects in the corners of the core in the analytical hysteresis model
- Underestimation of the magnetic flux density in the right hand corners of figure 4.13(b) may be corrected with a radial narrowing of the core (cf. figure 4.14).

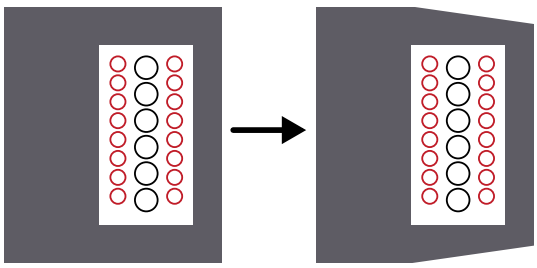

Figure 4.14.: Corrected (2D axisymmetric) core geometry

5. Operation of the Dual Active Bridge

To practically evaluate the designed and optimized transformer, a prototype is assembled and tested in the laboratory of the department LEA. For this purpose, a DAB converter as presented in figure 4.1 is assembled and taken into operation.

5.1. Transformer Prototype Assembly

According to the results from chapter 4, for the prototype DAB an integrated transformer is built up. To give an overview of the prototype transformer assembly, figures 5.1, 5.2 and 5.3 show 3D models of the core and the bobbin. The basis of the integrated transformer are two halves of a PQ40/40 core. One half remains unchanged, whereas the other half's middle leg is milled down. To reach the specified length of the upper core's middle leg, a small tablet needs to be manufactured. The most crucial part of the assembly is the stray path which is considered to be a cylinder in the axial symmetric simulations. To realize air gaps with a uniform thickness throughout the transition between the stray path and the outer core legs, the stray path is designed in such way that it clings to the PQ40/40 core's inner shape (see figure 5.3(b)). All milling actions are performed inhouse at the LEA laboratory with the Computerized Numerical Control (CNC) milling machine *Compact 350* from *imes-icore*.

For an integrated transformer, air gaps are necessary to adjust the electromagnetic properties. For the thermal design, air gaps mean a challenging task. Somehow, a thermal coupling of the magnetic core parts is needed to dissipate the heat caused by losses. Herein, the stray path tablet is the core part, that is most crucial in terms of

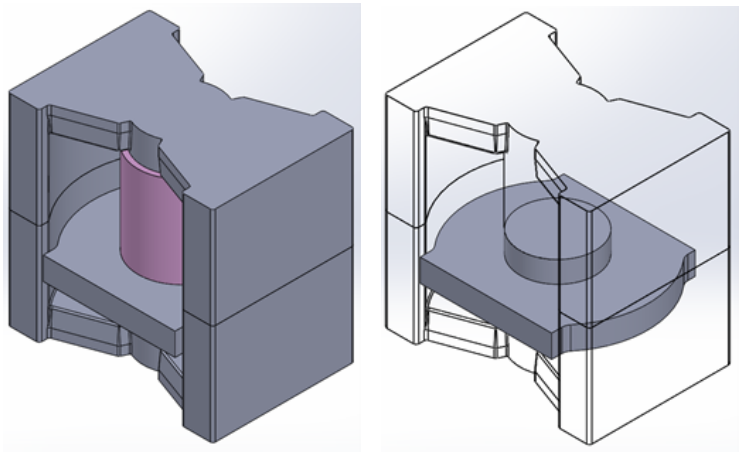

(a) Solid geometry (b) Wireframe geometry

Figure 5.1.: CAD model of the optimized core (3D perspective)

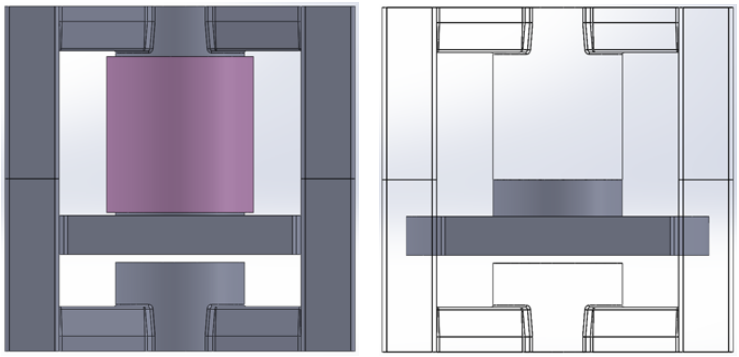

(a) Solid geometry (b) Wireframe geometry

Figure 5.2.: CAD model of the optimized core (2D side perspective)

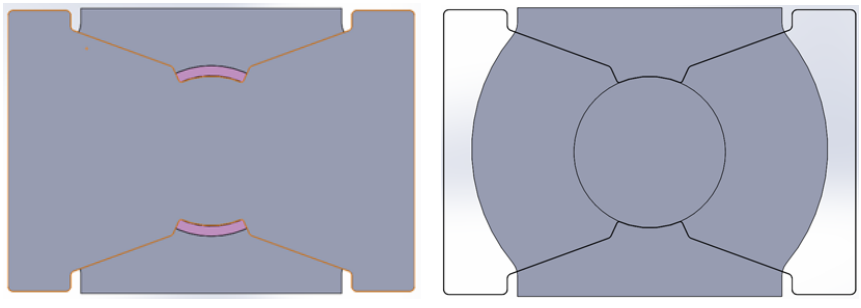

(a) Solid geometry (b) Wireframe geometry

Figure 5.3.: CAD model of the optimized core (2D top perspective)

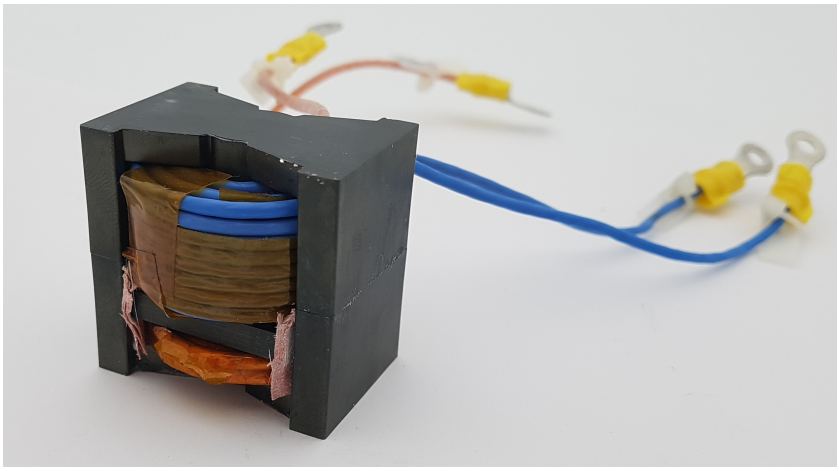

Figure 5.4.: Lab prototype of the integrated transformer

the thermal coupling. For this purpose, the heat can either be conducted to one of the transformers outer faces or can directly be dissipated via convection from the stray path's non-concealed surfaces. To enable good thermal coupling in the air gaps, the air gap according to R_{bot} (cf. figure 3.14) is filled with aluminum nitride spacers. Due to its brittleness, aluminum nitride is not suited for the curved air gap contour of the air gaps that realize the reluctance R_{stray} (cf. figure 3.14). Because of this, the two outer air gaps are equally filled with Thermal Interface Material (TIM). Since the length of the air gap according to R_{top} (cf. figure 3.14) is very small with 2.5 µm, the air gap is in the lab prototype omitted.

To assemble the windings of the transformer, a bobbin for the middle leg is drilled out of heat resistant Teflon (see figures 5.1(a), 5.2(a) and 5.3(a) - in purple).

5.1.1. Transformer Impedance Analysis

The transformer's impedance behaviour is investigated with the impedance analyzer *Wayne Kerr 6515B*.

L_{11}	683 µH
L_{22}	67 µH
L_{k1}	84 µH

Table 5.1.: Open and short circuit results

n	2.99
L_m	599 µH
L_s	84 µH

Table 5.2.: ECD parameters (cf. figure 3.9(b))

The parameters of the primary concentrated T-ECD (cf. figure 3.9) are determined with open and short circuit tests.

5.2. DAB Prototype System

To test the integrated transformer in a laboratory setup, a DAB converter is built up according to the block diagram 5.5. The eight SiC power MOSFETs are placed on a Printed Circuit Board (PCB), which is originally used for an LLC converter [21].

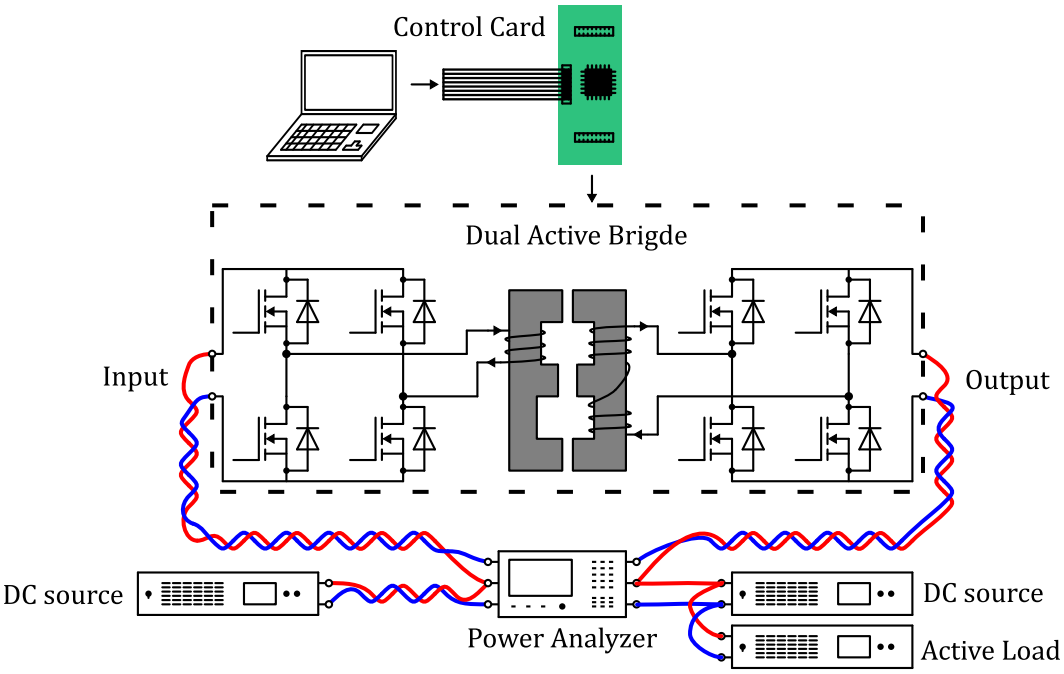

Figure 5.5.: Block diagram of the prototype system

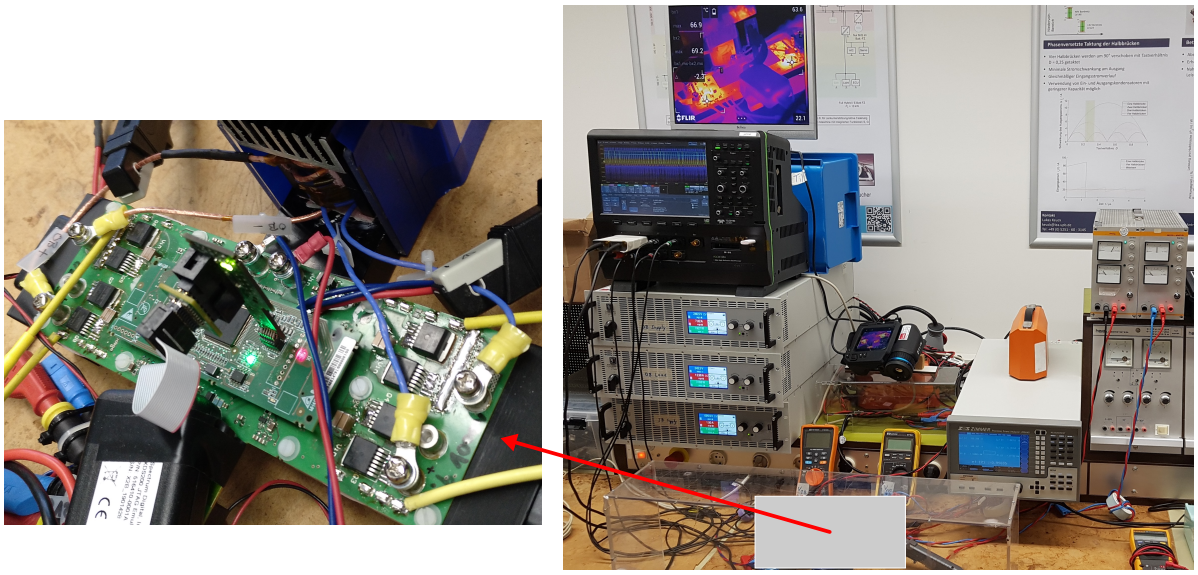

Figure 5.6.: Prototype system in LEA lab

The system is powered with a DC voltage source with 700 V on the input side. On the output side, a DC voltage source and an active load emulate a battery according to the system application (cf. figure 1.1) with a voltage range of 175 V to 295 V. The main card and the fans are supplied with external 14 V and 12 V power supply units. The control board, gate drivers and other periphery are supplied by an internal flyback converter. The control board is piggybacked on the main PCB.

To supervise the complete system an infrared (IR) camera is constantly monitoring the surface temperatures of the semiconductors and the transformer. For performance measurements a power analyzer monitors the input and output power as well as the efficiency.

5.2.1. Measurements and Validation

The basic functionality of the prototype system is shown with the scope figure 5.7. In none of the investigated working points saturation effects are observed.

To determine the system's efficiency, different working points of the prototype system

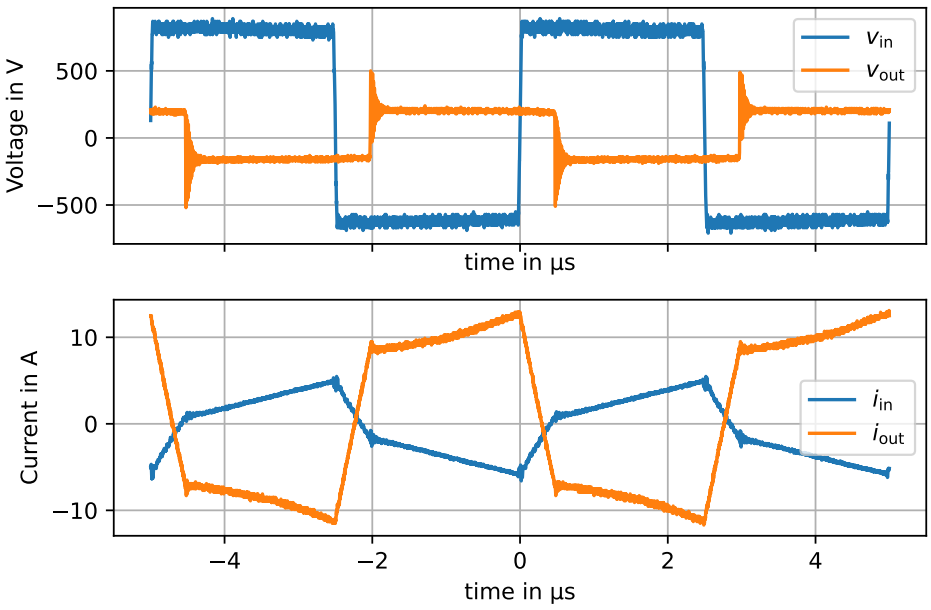

Figure 5.7.: Exemplary in-/output voltage and current waveforms of the DAB prototype system taken with *Tektronix MSO4104* oscilloscope (phase shift: 35° and $v_{out} = 175\,\mathrm{V}$)

Table 5.3.: Pairs of MOSFETs for the IB and OB of the DAB converter

	Input Bridge	**Output Bridge**
pair_1	C3M0120100J (CREE)	C3M0120065J (CREE)
pair_2	C3M0065100J (CREE)	C3M0060065J (CREE)

are investigated. The efficiency is measured in relation to the output power P_{out} with *Precision Power Analyzer LMG640* at minimal and nominal output voltage V_{out} and different dead time T_{dead}. However, the output power is controlled by variation of the phase shift. The maximum efficiency in the working point with nominal voltage and nominal output power is measured with about 96 %. Due to problems of EMI, the working point with maximal output voltage 295 V is not recorded at this early stage of the system built up.

Further, the thermal behaviour of the transformer is analyzed. Figure 5.9 shows the surface temperatures of the DAB assembly in steady state (after ≈ 25 min) in the working point with nominal power and nominal voltage. At an ambient temperature of about

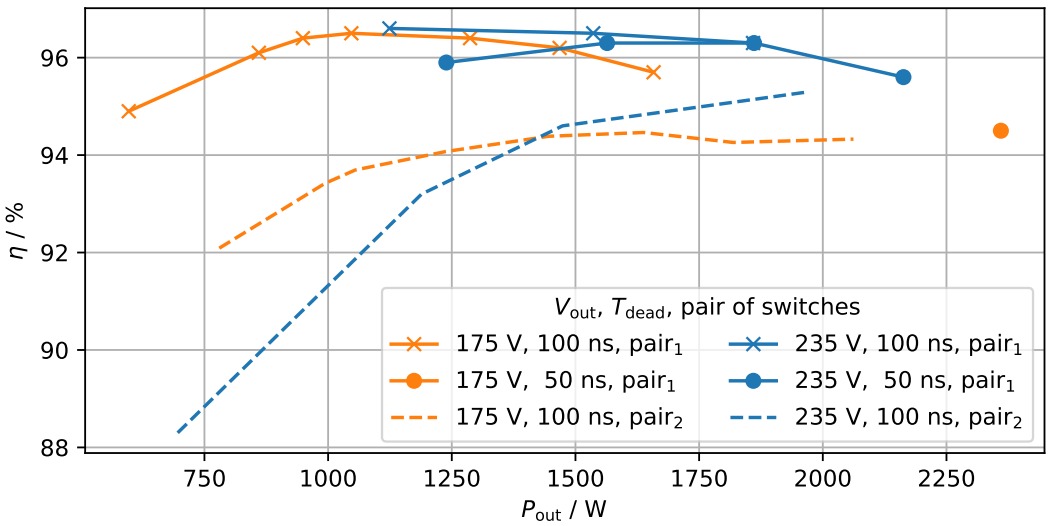

Figure 5.8.: Efficiency curves for minimal and nominal output voltage v_{out} at different dead times t_{dead} and MOSFET pairs (cf. table 5.3)

23 °C, the MOSFETs of the output bridge show a maximum temperature with 70 °C. The transformer has a surface temperature of 64.6 °C. The Polyethylene Terephthalate (PET) based *Mylar®* isolation of the windings limits the maximum allowed continuous stress temperature of the transformer assembly to 130 °C [22]. The loss optimal temperature for the core material N95 is specified in the datasheet with about 100 °C. The maximum temperature (Curie temperature) for N95 ferrite is even specified with > 200 °C. [23]

The comparatively good cooling system, with two heat sinks connected via TIM on the top and bottom side of the transformer and a fan with pressure chamber, keeps the temperature significantly below the thermal limits. In a practical application, the ambient temperature usually is higher and the thermal coupling worse, so that the heat deduction is reduced. As a consequence, the transformer's temperature in practical application may increase compared to the laboratory setup.

A close up of the warmed-up integrated transformer indicates, identifies the stray path as the hot spot (cf. figure 5.10). This behaviour corresponds to the theoretical consideration from section 5.1. The core parts close to the heat sink are identified to

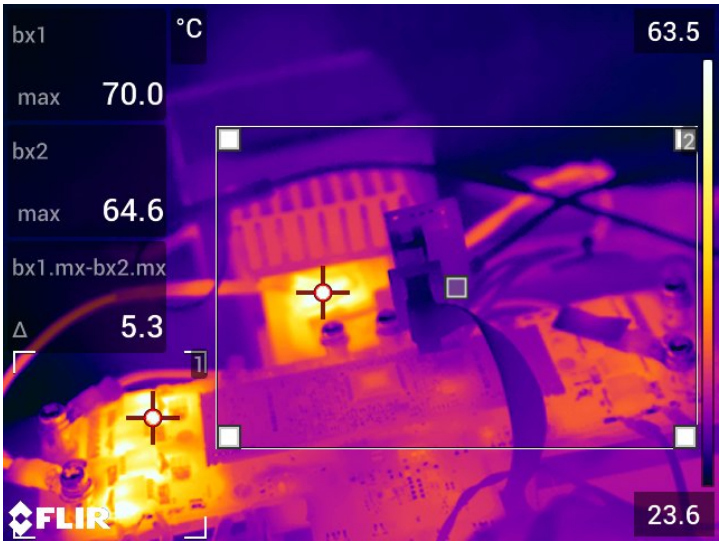

Figure 5.9.: Surface temperatures of the DAB at nominal power nominal voltage (2 kW and 235 V)

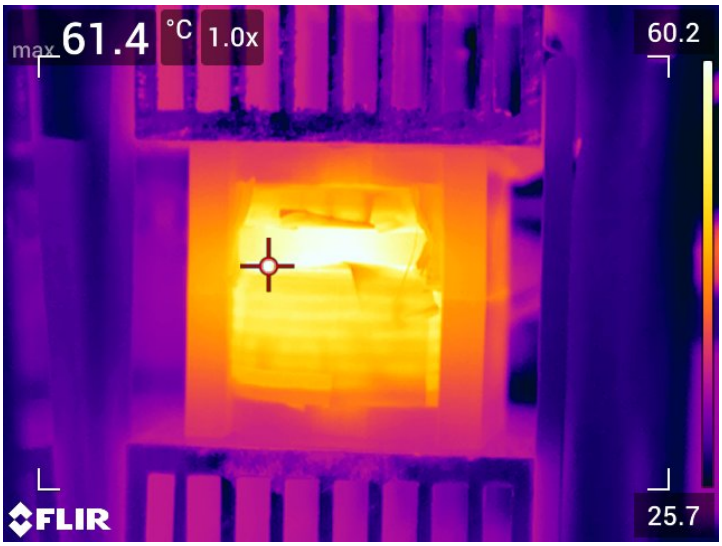

Figure 5.10.: Infrared Camera close up

be the coldest spots. This indicates, that there the thermal coupling via direct heat conduction into the heat sinks is better than on the side, where convection is directly cooling the ferrite core. The windings show lower temperatures than the stray path, which supports the results of the FEM simulation, that the winding losses are smaller than the core losses.

For a final validation of the transformer loss model, the measured losses of the prototype are compared with the transistor losses according to a circuit simulation. Therefore, the measured efficiency in the operation point with nominal output voltage and nominal output power is used to determine the total measured losses of the DAB converter. For the MOSFETs pair_2 (cf. table 5.3), at an input power of 2069.5 W and an output power of 1972.3 W, the total losses are 97.2 W.

	Transistor	Full Bridge (x4)
$\overline{p_{\text{sw, ib}}}$	3.6 W	14.4 W
$\overline{p_{\text{cond, ib}}}$	0.51 W	2.04 W
$\overline{p_{\text{sw, ob}}}$	10 W	40 W
$\overline{p_{\text{cond, ob}}}$	3.81 W	15.24 W
Transistor losses		71.68 W

Table 5.4.: Allocation of the transistor losses to their causes [18]

Transistor losses	71.68 W
Transformer losses	17.08 W
Simulated Losses	88.76 W
Measured Losses	97.2 W
Residual Losses	8.44 W

Table 5.5.: Allocation of the total losses to their causes

According to circuit simulations, taking into account incomplete ZVS, the losses of the MOSFETs are estimated with 71.68 W (cf. table 5.2.1)[18]. Adding the estimated 17.08 W losses of the transformer (cf. section 4.3.2), 8.44 W remain unallocated. On the one hand, losses in the layers of the PCB, the capacitors or the supply lines are included in the residual losses. On the other hand, both loss simulations are subjected to certain inaccuracy. It is not unlikely, that the transformer loss model underestimates the core losses. Especially the hysteresis losses may be higher according to non sinusoidal wave forms. Further, wave effects (cf. section 2.1) may increase the losses, as also observed in [6].

6. Abstract

In this work, a process for automated FEM based transformer design is presented. The entire design procedure is performed with the open source toolbox FEMMT from the department LEA at Paderborn University.

In terms of providing the required functionality, an approximation for stranded wires, a method for inductance calculation from field solutions, core loss models and an analytical reluctance model have been contributed to the toolbox. All functions are directly integrated into the Git repository.

Further, an exemplary design process for a transformer with dedicated leakage path is run through. By applying goal parameters, such as the transformer ratio, mutual and stray inductance as well as the current wave forms, a loss optimization for a wide input feature space is shown. Combining fast preliminary analytical and precise FEM based calculations, enables a fast investigation of a certain feature space. Moreover, a combination of initial global and subsequently local grid search approaches leads to a self converging optimization.

To validate the designed magnetic component, a laboratory prototype of the designed integrated transformer is assembled and put into operation in a Dual Active Bridge (DAB) converter. The bidirectional DAB is a part of an Uninterruptible Power Supply (UPS), that is capable of smart grid actions, by feeding back power to the mains. With the prototype converter a peak-efficiency of more than 96 % is achieved.

Bibliography

[1] Lukas Keuck, Frank Schafmeister, Joachim Böcker, Herbert Jungwirth, and Michael Schmidhuber.
"Computer-Aided Design and Optimization of an Integrated Transformer with Distributed Air Gap and Leakage Path for LLC Resonant Converter".
In: *PCIM Europe* (2019), pp. 122–129 (cit. on pp. 1, 28, 41).

[2] John David Jackson. *Klassische Elektrodynamik*. de Gruyter, 2006 (cit. on p. 3).

[3] *Ansys Maxwell*.
URL: `https://www.ansys.com/de-de/products/electronics/ansys-maxwell` (visited on 12/13/2021) (cit. on p. 3).

[4] *FEMM*. URL: `https://www.femm.info/wiki/HomePage` (visited on 12/13/2021) (cit. on p. 3).

[5] Stephan Koch.
"Quasistatische Feldsimulationen auf der Basis von Finiten Elementen und Spektralmethoden in der Anwendung auf supraleitende Magnete".
PhD thesis. TU Darmstadt, 2009 (cit. on pp. 3 sqq.).

[6] Lukas Keuck. "Entwurf eines einstufigen Ladewandlers auf Basis eines LLC-Resonanzwandlers (Unveröffentlicht)".
PhD thesis. Universität Paderborn, 2021 (cit. on pp. 6, 22–25, 28, 33 sq., 39, 67).

[7] *ONELAB*. URL: `https://onelab.info/` (visited on 08/18/2021) (cit. on pp. 7, 73).

[8] Christophe Geuzaine and Jean-François Remacle. *Gmsh*.
URL: `https://gmsh.info/` (visited on 08/18/2021) (cit. on pp. 7, 72).

[9] Patrick Dular and Christophe Geuzaine. *GetDP*.
URL: `https://getdp.info/` (visited on 08/18/2021) (cit. on pp. 7, 72).

[10] Korawich Niyomsatian, Johan Gyselinck, and Ruth V. Sabariego.
"Closed-form complex permeability expression for proximity-effect homogenisation of litzwire windings".
In: *IEEE TRANSACTIONS ON MAGNETICS* 41.5 (2005), pp. 1416–1419 (cit. on pp. 11, 13).

[11] Johan Gyselinck and Patrick Dular. "Frequency-Domain Homogenization of Bundles of Wires in 2-D Magnetodynamic FE Calculations".
In: *IET Science, Measurement Technology* 14.3 (2019), pp. 287–291 (cit. on pp. 12 sqq.).

[12] Prof. Dr.-Ing. Manfred Albach. *Induktivitäten in der Leistungselektronik*.
Springer Vieweg, 2017 (cit. on pp. 17, 19 sq.).

[13] David J. Griffiths. *Introduction to electrodynamics*. Pearson, 2018 (cit. on p. 18).

[14] Jonas Muehlethaler, Juergen Biela, Johann Walter Kolar, and Andreas Ecklebe.
"Core Losses Under the DC Bias Condition Based on Steinmetz Parameters". In: *IEEE TRANSACTIONS ON POWER ELECTRONICS* 27.2 (2012), pp. 953–963 (cit. on p. 25).

[15] Jonas Mühlethaler.
"Modelling and multi-objective optimization of inductive power components".
PhD thesis. ETH Zürich, 2012 (cit. on pp. 31 sq., 34).

[16] Richard P. Brent. *Algorithms for Minimization*. 1973 (cit. on p. 34).

[17] *brentq*. URL: `https://docs.scipy.org/doc/scipy/reference/generated/scipy.optimize.brentq.html` (visited on 11/29/2021) (cit. on p. 34).

[18] Nikolas Förster. *Simulations of a DAB (not published)*. 2021 (cit. on pp. 38 sq., 67).

[19] TDK Electronics. *PQ-Kerne und Zubehör*. URL: https://www.tdk-electronics.tdk.com/de/193506/produkte/produktkatalog/ferrite-und-zubehoer/epcos-ferrite-und-zubehoer/pqcores (visited on 11/30/2021) (cit. on p. 40).

[20] *quad*. URL: https://docs.scipy.org/doc/scipy/reference/generated/scipy.integrate.quad.html (visited on 11/29/2021) (cit. on p. 48).

[21] Lars Hankeln. "Entwicklung eines LLC Konverters mit Siliziumkarbid-Halbleitern für den Einsatz als 400V zu 12V Bordnetzwandler". MA thesis. Germany: Universität Paderborn, 2021 (cit. on p. 62).

[22] Gotthardt Isolierteile GmbH. *Isolierstoffklasse B*. URL: https://www.goba.de/wp-content/uploads/2020/06/Isolierstoffklasse-B.pdf (visited on 12/23/2021) (cit. on p. 65).

[23] EPCOS AG 2017 and TDK. *SIFERRIT material N95*. URL: https://www.tdk-electronics.tdk.com/download/528866/73730346930dfce60e468312e5e3023e/pdf-n95.pdf (visited on 05/02/2020) (cit. on p. 65).

[24] *LEA Python Toolbox*. URL: https://github.com/upb-lea/lea_python_toolbox (visited on 12/21/2021) (cit. on p. 74).

A. Acronyms

API Application Programming Interface

CNC Computerized Numerical Control

DAB Dual Active Bridge

ECD Equivalent Circuit Diagram

EMI Electromagnetic Interference

FEM Finite Element Method

FEMM Finite Element Method Magnetics (open source FEM tool developed by Ph.D. David Meeker)

FEMMT FEM Magnetic Toolbox (open source toolbox developed at LEA)

FFT Fast Fourier Transform

GetDP "General Environment for the Treatment of Discrete Problems"[9]

GMSH "three-dimensional finite element mesh generator with built-in pre- and post-processing facilities"[8]

GUI Graphical User Interface

HF High Frequency

IB Input Bridge

iGSE improved Generalized Steinmetz Equation

IR infrared

LEA Department of Power Electronics and Electrical Drives

MMF magnetomotive force

MOSFET metal–oxide–semiconductor field-effect transistor

MQS magnetoquasistatic

OB Output Bridge

ONELAB "Open Numerical Engineering LABoratory"[7]

PCB Printed Circuit Board

PET Polyethylene Terephthalate

PyPI Python Package Index

RMS Root Mean Square

SiC Silicon Carbide

T-ECD T -(shaped) Equivalent Circuit Diagram

TIM Thermal Interface Material

UPS Uninterruptible Power Supply

VCS Version Control System

ZVS Zero Voltage Switching

B. Appendix

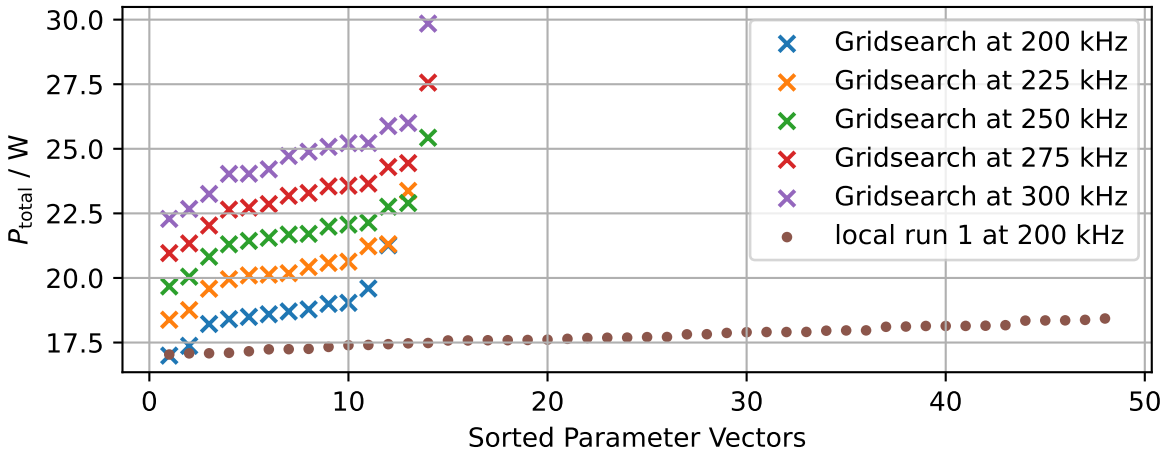

Figure B.1.: Total losses of the final parameter set S_{final} (cf. figure 4.10) within the optimization procedure (raw data)

B.1. Impedance Curves

The impedance curves are extracted and post processed with functions of the LEA Python Toolbox [24]. The measurement of the primary side with secondary side open (to determine L_{11}) is shown in figure B.2. The resonant frequency is with 1.2 MHz clearly above the switching frequency of 200 kHz.

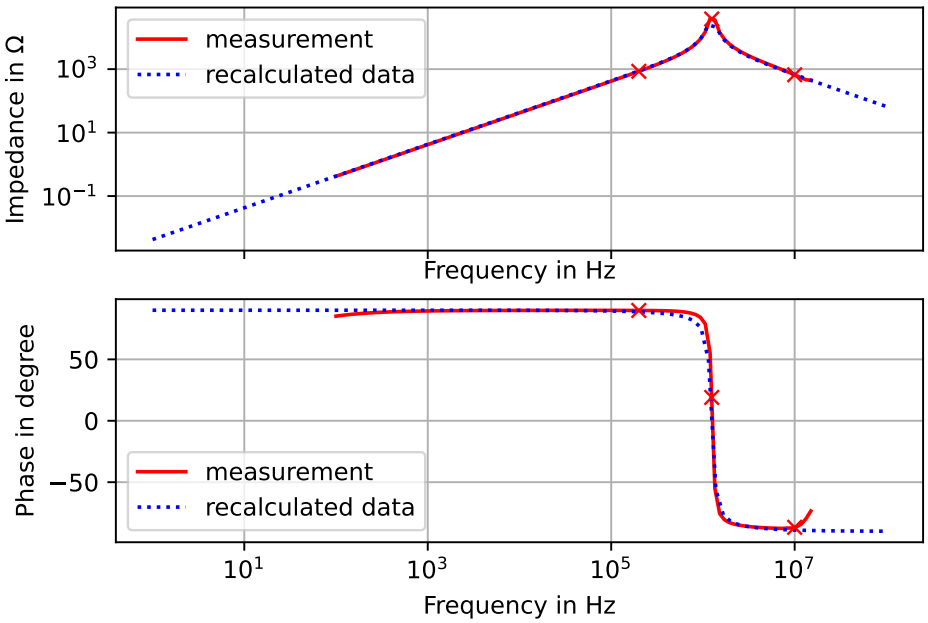

Figure B.2.: Open circuit measurement on the primary side

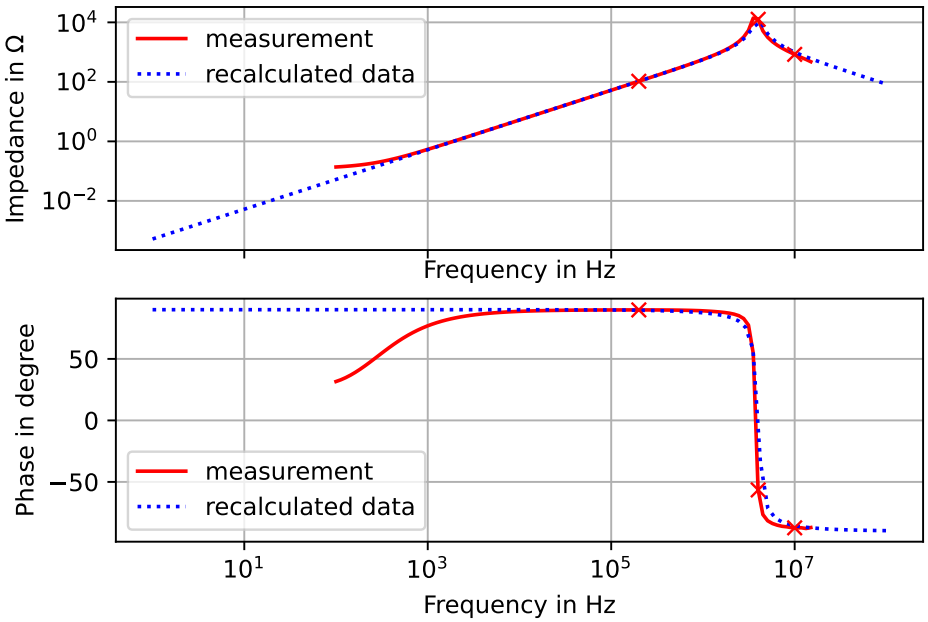

Figure B.3.: Short circuit measurement on the primary side

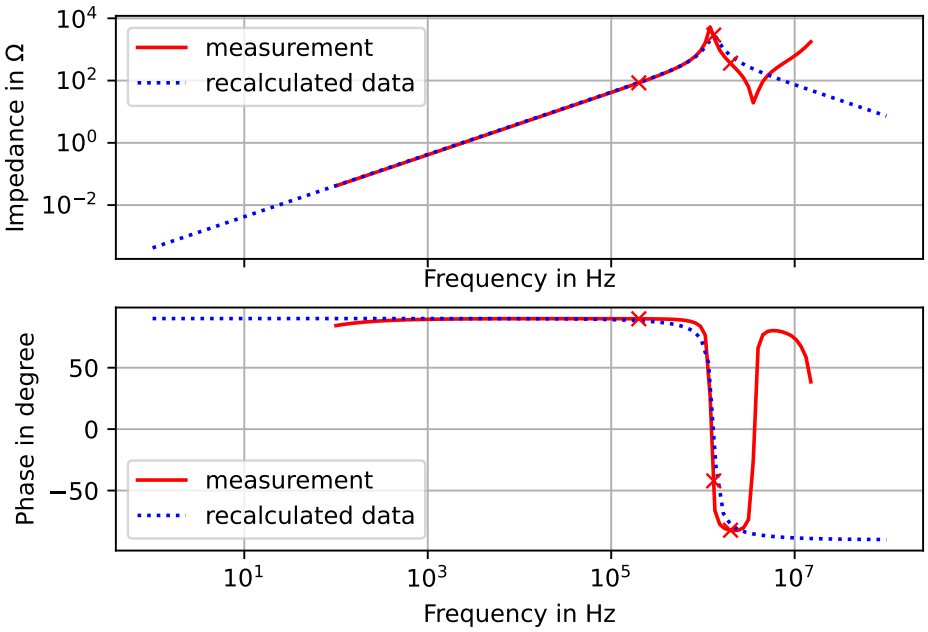

Figure B.4.: Open circuit measurement on the secondary side

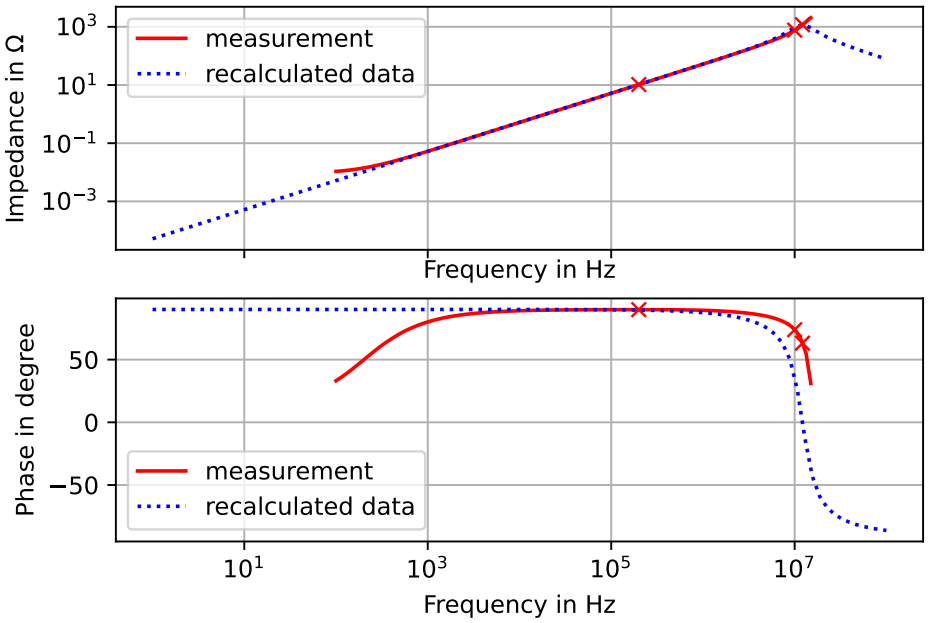

Figure B.5.: Short circuit measurement on the secondary side